SLAC–PUB–5753
February 1992
(I)

A Precise Calibration of the SLAC 8 GeV Spectrometer Using the Floating Wire Technique*

L. Andivahis[1], F. S. Dietrich[2], C. W. Johnson[2(a)], A. Lung[1], G. G. Petratos[3,4(b)]
K. Van Bibber[2] and L. W. Whitlow[2,5(c)]

[1] *The American University, Washington, DC 20016*
[2] *Lawrence Livermore National Laboratory, Livermore, CA 94550*
[3] *University of Rochester, Rochester, NY 14627*
[4] *Stanford Linear Accelerator Center*
Stanford University, Stanford, CA 94309
[5] *Stanford University, Stanford, CA 94305*

Condensed version submitted to Nuclear Instruments & Methods

---

* Work supported by Department of Energy contracts DE–AC03–76SF00515 (SLAC), DE–AC02–ER13065 (U.R.), W–7405–ENG–48 (LLNL), and National Science Foundation grant PHY85-10549 (A.U.).
(a) Present address: California Institute of Technology, Pasadena, CA 91125
(b) Present address: Stanford Linear Accelerator Center Stanford, CA 94309
(c) Present address: Daikin Industries, Tsukuba–City, Ibaraki, Japan

Abstract

The SLAC 8 GeV/c spectrometer was optically calibrated using the floating wire technique. The forward and reconstruction optics coefficients were measured as a function of spectrometer momentum. The point–to–point uncertainty for the large, first–order coefficients was ± 0.4% or better, with an absolute normalization uncertainty of ±1.0%. These coefficients were used to determine the momentum dependence of the acceptance, and to constrain a newly developed TRANSPORT model of the spectrometer which reproduces the measurements to within their errors. The central momentum, P_c, was measured for fourteen nominal set–points to ±0.025% absolute uncertainty. A linear fit to measured central momenta and corresponding dipole NMR field measurements gives $P_c = 0.41511B + 0.00054$, where B is the magnetic field of the dipoles in kG, and P_c is in GeV/c.

1. Introduction

This report gives a comprehensive summary of the optical properties of the SLAC 8 GeV† spectrometer as determined via the floating wire measurements taken during the fall and winter of 1986. There are four chapters followed by four appendices. Chapter one motivates the need for new measurements, describes the basic optical properties of the 8 GeV spectrometer and underlines the principles of the floating wire technique. Chapter two focuses on the hardware designed and built for the measurements, and on the method used to make the measurements, with emphasis placed on error minimization and determination. In chapter three the analysis procedures are outlined and the results are presented. The final chapter contains comments and concluding remarks.

1.1 Background and Motivation

With a new generation of high precision experiments being undertaken, precise knowledge of the 8 GeV spectrometer optical characteristics is required. Measuring cross sections to ± 1.0%, as in SLAC experiments E140[1-3] and NE11,[4] requires knowing the acceptance or solid angle to an equal precision, and determining the central momentum to at least ± 0.1%. Previous studies of the 8 GeV optics, the dark–current[5,6] calibration in 1968, and the jailbar[7] calibration in 1984, which relied on fitting electron beam data, yielded relatively large uncertainties in the optics coefficients when systematic effects were folded in. Also, the dark current data indicated a rather strong momentum dependence[5] to some of the optics coefficients. Since experiments E140 and NE11 measured cross sections at various kinematics, any momentum dependence of the acceptance had to be well understood, and corrections made to account for it.

† For convenience, the units GeV/c will be written as GeV throughout this report.

A new set of measurements was needed which could determine the optics coefficients and the central momentum to high precision over a wide range of spectrometer momenta. The precision of the large, first–order coefficients, which are inversely proportional to the spectrometer acceptance, had to be better than ± 1.0% in order to determine the acceptance equally as well. Accomplishing these goals meant minimizing systematic effects and having a full understanding of the errors and any correlations when determining the uncertainties in the final results.

The decision to use the floating wire technique instead of the electron beam in a new optical study was made based on the level of precision and control offered by this technique. With a floating wire the entrance and exit trajectories of the simulated particle are directly measurable; in particular there is no guess-work involved regarding the position of the input trajectory. The result is that a set of optics coefficients can be obtained from a least squares fit to the measured elements of the input and output vectors. This is contrary to the situation one has in an electron beam study using the jailbar[7] technique where an initial optics matrix must be assumed and an iterative process undertaken until the reconstructed quantities satisfy reasonable distributions at the jailbar grid. In addition, the floating wire method provides a means of calibrating the spectrometer momentum independent of the beam energy. Before describing the measurements in detail it is useful to describe the apparatus on which the measurements were made and the quantities being measured.

1.1.1 The Apparatus—The 8 GeV Spectrometer

The SLAC 8 GeV spectrometer[8] is one of three magnetic spectrometers in End Station A designed for fixed target electron scattering experiments with extended targets. It is free to rotate about a central axis, known as the pivot, and spans an angular range of roughly 11.5 to 100 degrees. The spectrometer consists of five magnets. From pivot to detector hut these are: Q81 and Q82, two quadrupoles for initial focusing of incoming particles; B81 and B82, two 15 degree vertical bend magnets which provide the momentum dispersion; and Q83, a quadrupole for final focusing

before the particles reach the hut. The overall path length for a particle traversing the magnetic center of the spectrometer is nearly 15 meters from the entrance face of Q81 to the exit face of Q83. Figure 1.1 illustrates the layout of the spectrometer.

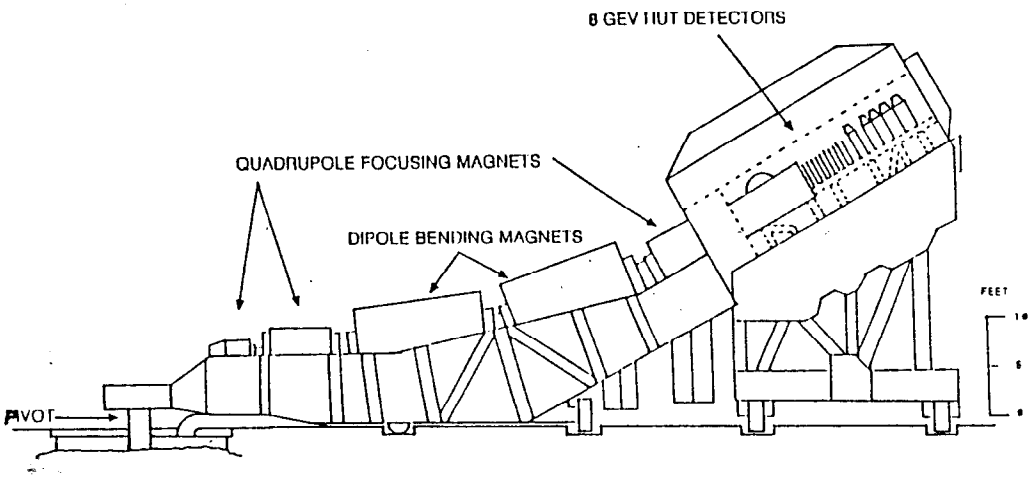

Figure 1.1. The 8 GeV spectrometer in End Station A.

The optics[9] for the 8 GeV spectrometer have been optimized to accommodate long targets, while simultaneously maximizing both the solid angle and the momentum resolution. This means allowing for particles which can scatter from any point along the length of the target. Thus, in the horizontal plane the focusing is line–to–point so that particles scattering with the same angle theta, but from different points along the length of the target, will be focused to the same point in the theta focal plane in the hut. On the other hand, in the vertical plane the focusing is point–to–point. Due to large chromatic aberrations, the momentum focal plane is tilted at an angle of 13.9 degrees with respect to the central ray. It is located† roughly half a meter behind the theta focal plane. Particles leaving the target with like momenta but varying vertical angles, phi, are focused to the same point in this plane. Figure 1.2

† Results of this study indicate otherwise, see section 3.2.4.

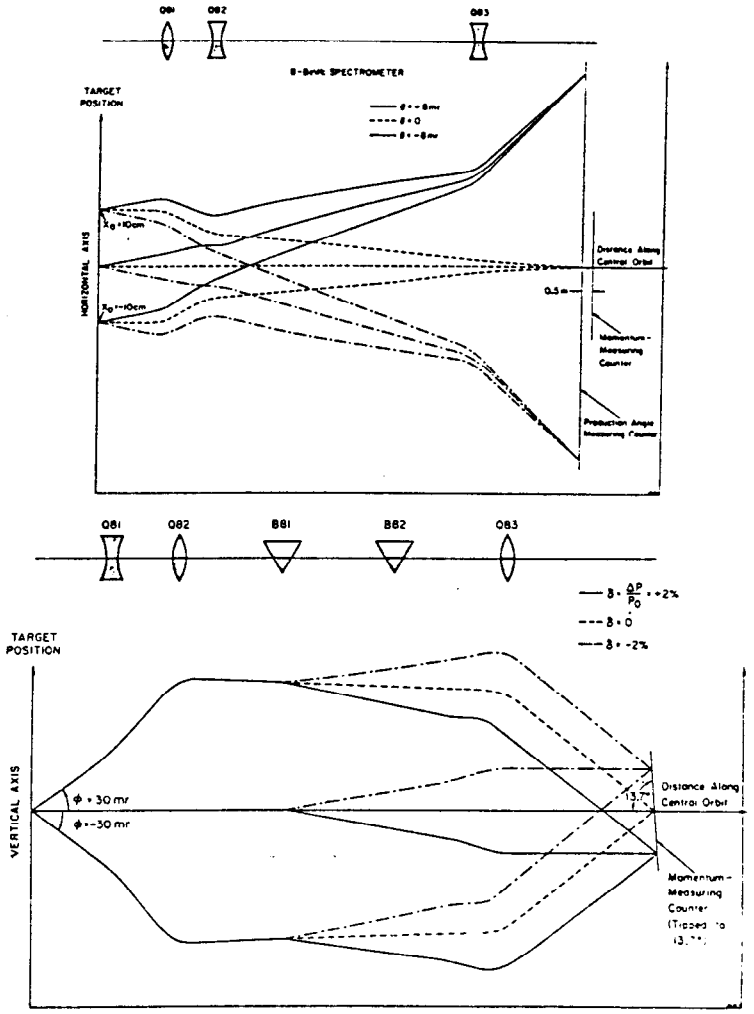

Figure 1.2. The focal properties of the 8 GeV spectrometer. The upper diagram shows the first order horizontal focusing properties, while the lower diagram shows the first order vertical focusing properties.

illustrates the horizontal and vertical focusing properties of the 8 GeV.

The 8 GeV has a acceptance of approximately 0.7 msr by 10% in momentum with a momentum resolution of 0.05%.[10] The solid angle is nominally given by the following ranges:

$$\theta \simeq \pm 8 \text{ mr}$$

$$\phi \simeq \pm 28 \text{ mr}$$

$$\delta \simeq \pm 5 \text{ \% .}$$

1.1.2 *The Coordinate System*

The coordinate system used in the measurements was a right handed system oriented such that $\mathbf{z}^{\dagger}$ points along the trajectory corresponding to a central ray, **x** points to the left of a central ray, and **y** is orthogonal to the **x**–**z** plane and points upward. A central ray is defined as a particle which passes through the magnetic centers of the magnets, and thus has a momentum equal to the central momentum of the spectrometer. This coordinate system coincides with that of TRANSPORT,[11,12] a program used in designing beam transport systems. However, in TRANSPORT a bending magnet is defined to bend in the **x**–**z** plane, and specifically toward the **-x** direction. Thus, a rotation of $-90°$ must be applied to the dipole magnets when using TRANSPORT to accommodate the 8 GeV bend plane bending in the **y** plane. See, for example, the TRANSPORT model given in section 3.2.4.

Within this cartesian system, a particle's instantaneous position is given in terms of six coordinates. These represent deviations of the respective coordinate from the central trajectory. The six coordinates are defined below and illustrated in Figure 1.3.

- x — displacement along the **x** axis of a particle with respect to the central ray,
- θ — angle the particle makes in the **x**–**z** plane with respect to the central ray,
- y — displacement along the **y** axis of the particle with respect to the central ray,
- ϕ — angle the particle makes in the **y**–**z** plane with respect to the central ray,
- l — difference in path length between the particle and a central ray trajectory for a given value of z,
- δ — fractional momentum deviation of the particle from the

† Throughout this report the convention for denoting coordinates is as follows: **z** refers to the generic coordinate axis, z refers to a specific value of the respective coordinate in the right–handed system described above, and $\tilde{z}$ refers to coordinates in a right–handed system centered on tooling ball B of Q83.

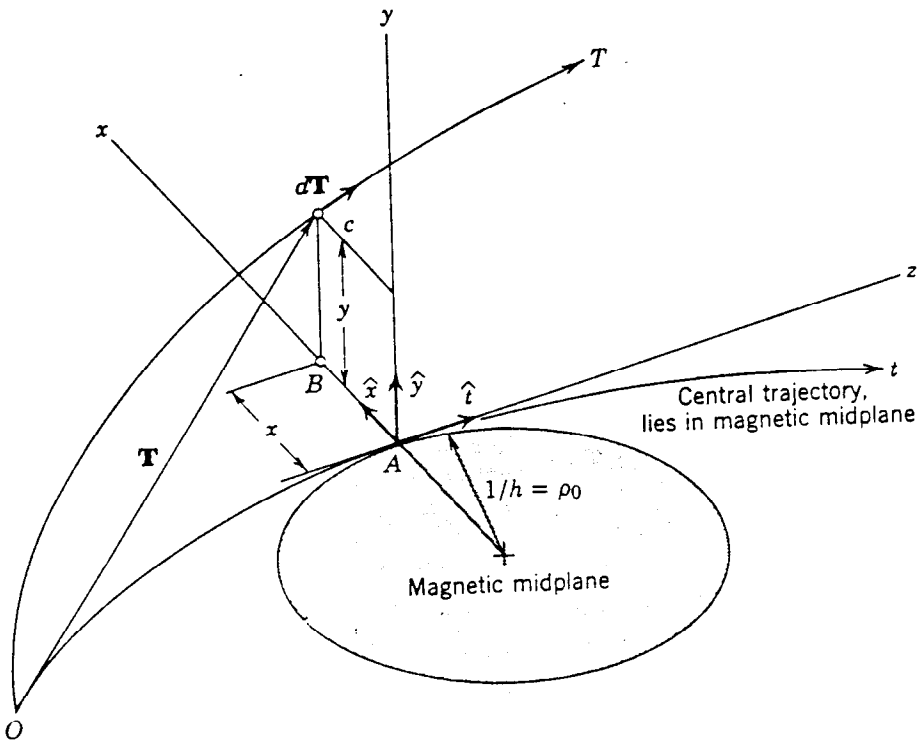

Figure 1.3. The coordinate system. The TRANSPORT coordinate system is a right handed system in which a particle's position is represented by deviations from the central trajectory path.

central ray trajectory; $\delta \equiv (P - P_o)/P_o$ where P_o is the central momentum.

Distances are in centimeters, angles in milliradians and δ is in percent. Notice that z is not used explicitly but is replaced by the variable l.

1.1.3 The Measured Quantities—The Optics Coefficients

TRANSPORT simulates the effects of a given beam transport system on charged particles traversing it through the use of matrix multiplication.[11] If we associate with each element, i, of the spectrometer (*i.e.* magnet, drift space *etc.*) a matrix $\mathbf{M}_i$ which characterizes the effect on a charged particle traversing the element, then we can represent the entire spectrometer by a matrix $\mathbf{M}_s$ which is the product of the

matrices $\mathbf{M}_i$, thus

$$\mathbf{M}_s = \prod_i \mathbf{M}_i. \tag{1.1}$$

In principle $\mathbf{M}_s$ embodies all the information we need to know about the focusing properties of the spectrometer: its elements are the coefficients of a Taylor expansion about the central ray trajectory, and they are known as the TRANSPORT coefficients or more generally optics coefficients. If we let $\mathbf{Q}$ denote the initial coordinate vector of the particle,

$$\mathbf{Q} \equiv \{x_o, \theta_o, y_o, \phi_o, l_o, \delta\}, \tag{1.2}$$

and $\mathbf{q}$ the final coordinate vector,†

$$\mathbf{q} \equiv \{x_f, \theta_f, y_f, \phi_f, l_f, \delta\}, \tag{1.3}$$

then we can write down the following transformation which relates the initial coordinate vector to the final coordinate vector via the TRANSPORT coefficients, the elements of $\mathbf{M}_s$:

$$\mathbf{q} = \mathbf{M}_s\ \mathbf{Q}. \tag{1.4}$$

This is referred to as the *forward* transformation as it transports a particle from the target point to the detector hut. A *reverse* transformation can also be expressed as follows:

$$\mathbf{Q} = \mathbf{M}_s^{-1}\mathbf{q}, \tag{1.5}$$

where $\mathbf{M}_s^{-1}$ contains the reverse TRANSPORT coefficients, those necessary to take a particle from the detector hut back to the target.

In this study, the Taylor expansion is taken out to second order. Standard notation has been developed to represent the expansion and it is useful to introduce it here as the results will be quoted in terms of this notation. Thus, to second order the expansion can be written explicitly as follows:

$$q_k = \sum_{i=1}^{6} \langle q_k | Q_i \rangle Q_i + \sum_{i=1}^{6} \sum_{j=1}^{i} \langle q_k | Q_i Q_j \rangle Q_i Q_j, \tag{1.6}$$

† Note that δ remains constant due to energy conservation.

where Q_k and q_i are the elements of the coordinate vectors $\mathbf{Q}$ and $\mathbf{q}$ respectively. The quantities $\langle q_k|Q_i\rangle$ and $\langle q_k|Q_iQ_j\rangle$ are the first and second order optics coefficients respectively, where for example, $\langle q_1|Q_2\rangle \equiv \langle x_f|\theta_o\rangle$. Interchanging q and Q will give the expression for the reverse transformation.

1.1.3.1 The Significance of Reconstruction Coefficients

In an experiment it is the final coordinate vector of the scattered particle which is measured in the detector hut. The initial coordinate vector at the scattering point within the target needs to be determined via the reverse transformation. A complication arises however, since only the particle's position and angles are measured, x_f, y_f, θ, ϕ, but not the particle's relative momentum, δ. For most experiments in ESA the particle's path length deviation from the central ray, l_f, is not measured, but neither is it needed in analysis. Thus l is omitted from the elements of the coordinate vectors. In rare cases where time of flight information is needed, and thus l is needed, one must rely on TRANSPORT models or ray traces for these coefficients as they have not been measured. The relative momentum is vital however, and to determine it, a constraint, $y_o = 0$, is placed on the system[7]. This is consistent with the fact that the spread in beam height at the target is small, and it allows one to solve for δ in terms of the four remaining coordinates. With this constraint applied, and omitting l, the expressions for the coordinate vectors reduce to:

$$\mathbf{Q} \equiv \{x_o, \theta_o, \phi_o, \delta\}, \tag{1.7}$$

$$\mathbf{q} \equiv \{x_f, \theta_f, y_f, \phi_f\}, \tag{1.8}$$

and the transformation equation is given as:

$$\mathbf{Q} = \mathbf{R}_s\mathbf{q}. \tag{1.9}$$

The coefficients of the matrix $\mathbf{R}_s$ are called *reconstruction* coefficients, as they are used to reconstruct the target scattering coordinates in practice. There is a relationship

between a subset of the reverse TRANSPORT matrix elements and the reconstruction matrix elements, *i.e.* one can express one set of coefficients in terms of the other. The equations relating the two sets of coefficients can be found in Appendix A.

The set–up for the floating wire calibration was designed to optimize the determination of the forward and reconstruction coefficients.

1.2 The Floating Wire Technique

A current–carrying wire suspended under tension was used to simulate the trajectory of a charged particle traversing the spectrometer. This technique is known as "The Floating Wire Technique"[13,14] and is a standard method used to calibrate magnets when mapping the magnetic field is not a viable option.

For a wire to assume the same trajectory as a charged particle implies the equivalence of the equations of motion governing a massless, current carrying wire under tension in a magnetic field, and a charged particle traversing the same magnetic field. Figure 1.4 shows the forces acting on the wire and an electron traveling with initial velocity $\vec{v}_o$, both in the presence of a uniform magnetic field $\vec{B}$.

Summing the forces on the wire, and neglecting the force due to gravity gives the following relation for a wire in equilibrium:

$$\frac{T}{I} = \rho_w B \ . \tag{1.10}$$

For an electron experiencing constant acceleration in the presence of a magnetic field, we can write:

$$\frac{P}{e} = \rho_e B \ . \tag{1.11}$$

For the wire to assume the same trajectory as the electron requires $\rho_w = \rho_e$. This leads to the floating wire relationship:

$$\frac{T}{I} = \frac{P}{e}. \tag{1.12}$$

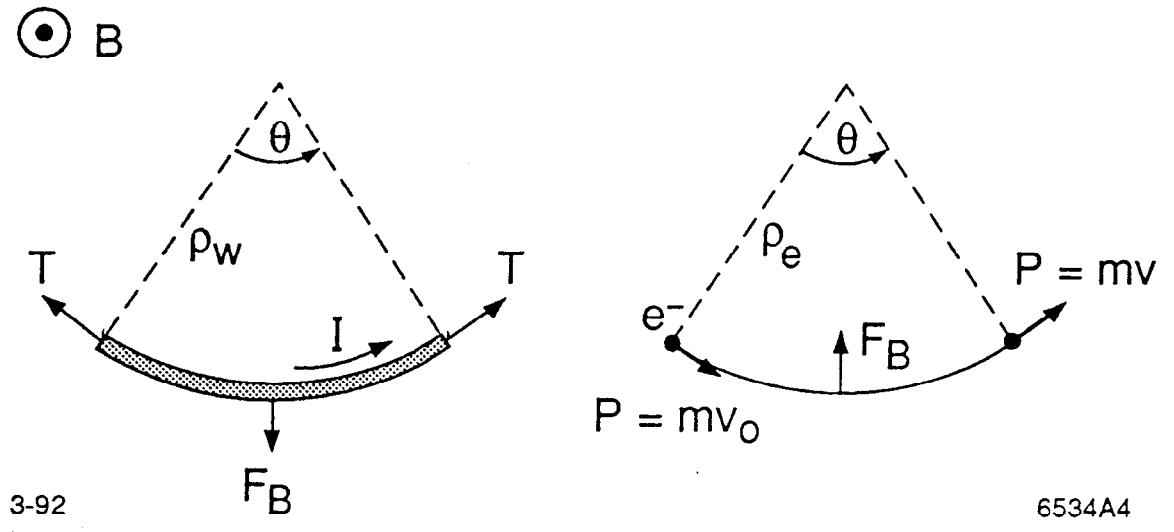

Figure 1.4. Force diagram for a wire and an electron in a magnetic field. The wire carries a current I and has a radius of curvature ρ_w. The electron has an initial momentum given by $\vec{P} = m\vec{v}_o$, and has a radius of curvature ρ_e.

For T in g, I in A, and P in GeV/c, this becomes†

$$P = (2.93770 \times 10^{-3})\frac{T}{I}. \tag{1.13}$$

† The local value for the acceleration due to gravity, $g = 979.914$ cm/sec^2, has been used.

2. Apparatus and Data Sample

The floating wire calibration was designed to achieve a precision of ± 0.05% in the calibration of the central momentum and ± 0.5% in the determination of the large, first order optics coefficients. For each trajectory several quantities had to be measured: the tension on the wire, the current in the wire, and the position of the entrance and exit trajectories. In addition, the wire current had to remain constant to within 0.01%. To ensure stability and measurability of the system within the desired precision new apparatus was designed and built. These included a current regulator with a response time in the millisecond range, as well as position measurement frames which located the wire position electromagnetically. The air–bearing pulley was the only acquired piece of equipment and it was studied extensively to fully understand how it affected the applied tension. The following sections describe these items[15] emphasizing those aspects which were crucial to minimizing the uncertainties. Section 2.2 gives the uncertainties in each of the measured quantities, tension, current, and position, and discusses how they affect and limit the precision of the calibration. The last section describes the data collection procedure and the range of data obtained.

2.1 Floating Wire Apparatus

A 0.0127 cm diameter copper–beryllium wire of linear density $\rho = 0.001082$ g/cm was anchored roughly 152 cm upstream of the momentum focal plane in the detector hut. The wire passed through the spectrometer beam pipe and over an air–bearing pulley located at the pivot. The tension in the wire was supplied by a known weight which hung from the wire as it passed over the pulley. Two weights, nominally 410 g and 100 g were used to span a range in momenta from 0.5 GeV to 9.0 GeV. A 160 V Tucker power supply provided the current in the wire, which was measured using a HP 3468A DVM to record the voltage drop over a calibrated shunt. The currents

ranged from 0.07 A for the 100 g weight at 4 GeV, to 0.6 A for both the 100 g weight at 0.5 GeV and the 400 g weight at 2 GeV. A fast current regulator with a sensitivity of 0.01% in a range of 0.05 A to 1.5 A was used to counter any noise arising from air currents induced by joule heating, thus maintaining a constant current in the wire to 0.01%. Figure 2.1 illustrates the setup.

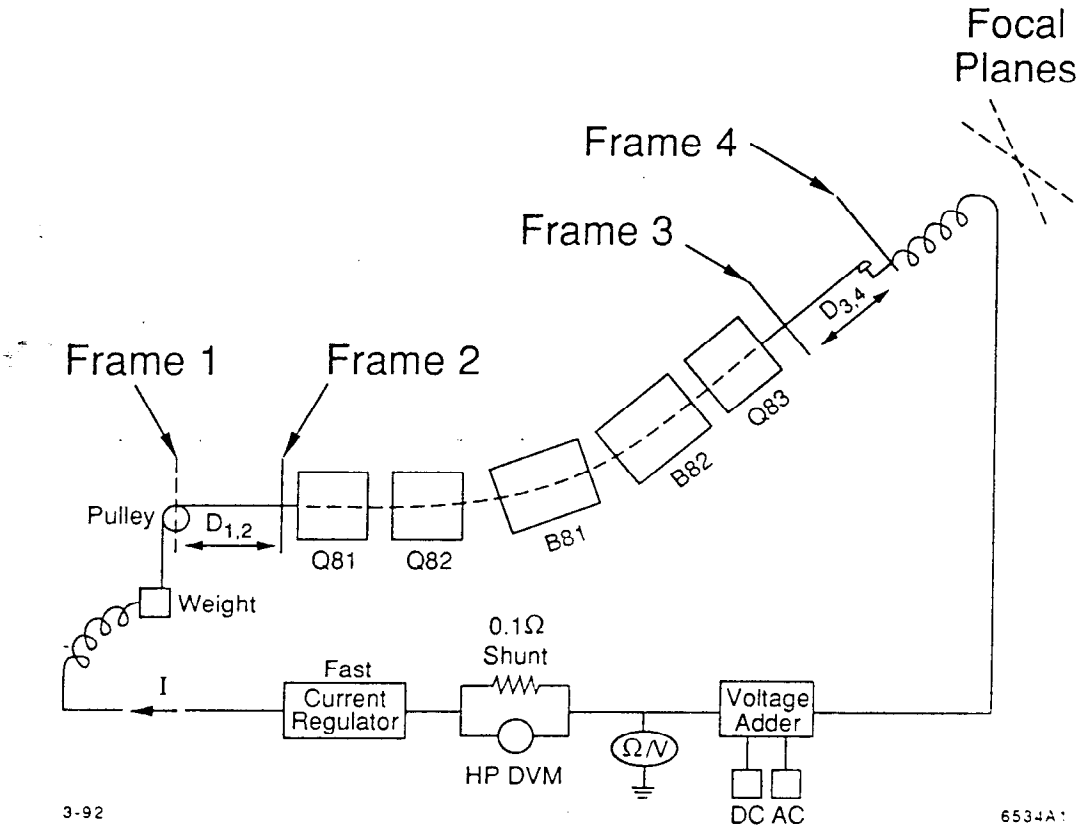

Figure 2.1. Schematic of the wire float apparatus. In the detector hut the Cu–Be wire is fastened to a "half-pulley" free to rotate about a vertical axis. The pulley is anchored to a pin which is placed into grid holes in Frame 4. At the target, the wire runs over the air-bearing pulley and is attached to the hanging weight. The resistive load in the Cu–Be wire is roughly 150 Ω.

The entrance and exit trajectories of the wire were measured using four frames

mounted transverse to the wire path. These were referred to as Frame 1 and Frame 2 at the spectrometer entrance, and Frame 3 and Frame 4 in the hut. The outer two frames, 1 and 4, represent the planes in which the wire endpoints lie. The position of the endpoint in the hut was limited to a grid of one inch spacings in both **x** and **y**. The target endpoint could be positioned continuously in **x**, while the **y** position remained fixed at beam height in keeping with the constraint that $y_o = 0$. The two inner frames, 2 and 3, were similar and determined the wire position electromagnetically. Cylindrical "position sensors" within each frame, containing inductors, relied on a 25 kHz frequency AC current superimposed on the wire to indicate when the movable cylinder was electrically centered about the wire. The cylinder location in **x** and **y** was then recorded. Operation of the sensors is described below.

The frames allowed the position of the trajectory to be determined relative to the arbitrary coordinate system within each frame. These arbitrary positions had to be converted into displacements in a TRANSPORT coordinate system. The frames were carefully surveyed to determine the relationship between the internal coordinate system of each frame, and that of TRANSPORT. Details of the survey are described in Appendix B.

2.1.1 Pulley Assembly

The pulley wheel[16] had an axle with spherical bearings on each end. The bearings rested in cups through which pressurized air flowed, as shown in Figure 2.2. The angle, γ, at which the wheel had to be supported by the cups such that the net force was directed into the cups was a function of the applied tension, and was given by

$$\gamma = \arctan\Big(\frac{M_T}{M_T + M_P}\Big), \tag{2.1}$$

where M_T is the mass supplying the tension and M_P is the mass of the pulley wheel. Dry nitrogen gas was used to supply the pressure as "house air" was found to contain too much dirt and oil, requiring frequent cleaning of the bearings. The angles and pressures required for the tensions used are given in Table 2.1. If the pressure was

too low, the circuit shorted to ground when the bearings contacted the cups and the wire would not float.

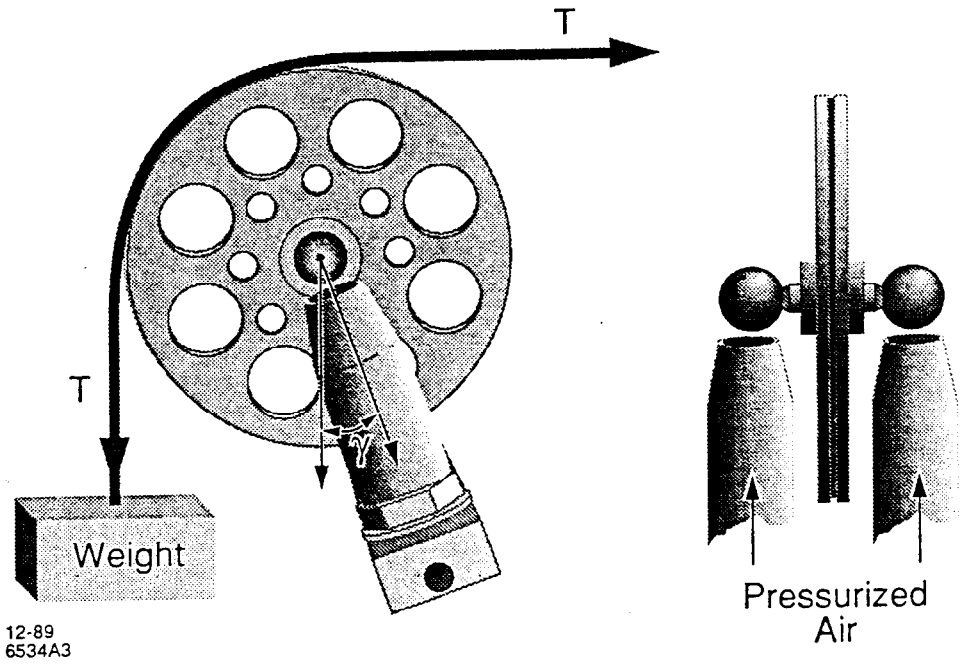

Figure 2.2. The air-bearing pulley. The pulley was originally built for the wire float of the 1.6 GeV spectrometer. The bearings and cups were cleaned and polished for re-use.

Knowledge of the tension in the wire required a full understanding of the air-bearing pulley. Since the pulley was not completely balanced, it introduced a small additional tension in the wire. The problem was complicated by the fact that the magnitude of this induced tension was dependent on the orientation of the pulley wheel bearings within the cups. This was a direct consequence of the non-uniformities in the surfaces of the bearings and cups, which even a cushion of air flowing between the surfaces could not remedy. It might be possible to reduce this problem in the

Table 2.1. Properties of the Air–Bearing Pulley. To guarantee a float, it was best to over–pressure the pulley first and then bring it down to its set point. The over–pressure values are given in parentheses.

Tension	γ	Pressure
410 g	37.6°	30 (50) psi
100 g	24.2°	15 (50) psi

future by using a pulley with a cylindrical axle thereby mitigating the difficulties inherent in constructing two identical, perfectly spherical bearings.

In studying the pulley, we were able to greatly reduce the initial dependence of the induced tension on wheel orientation, and obtain a measure of the resultant effect. By placing pieces of tape on the wheel at a specific location we were able to balance the pulley, thereby flattening out the sinusoidal shape of the dependence, leaving a nearly constant tension, independent of wheel orientation. Figure 2.3 illustrates the initial effect, indicated by the crosses, and the final effect, shown by the diamonds, when the wheel was balanced. These measurements were made by maintaining a constant current in the wire and recording the y position of the wire at Frame 1, each time rotating the wheel position in the cups. If the induced tension was independent of position of the bearings within the cups, then one should see no change in the y position at Frame 1. This technique had to be repeated for the 100 g and 410 g weight since the location of the place to add tape depended on γ.

To measure the magnitude of the resultant induced tension[16] the pulley was removed from the pivot and set up as an Atwood's machine. Two equal masses, m, were hung, one from each side of the pulley. A small weight, m_o, where $m_o \ll m$ was alternately placed on each side of the pulley and the time, t, required for the mass, $m + m_o$, to fall a distance h was recorded. This was repeated many times while varying the initial wheel orientation in the cups. The equation of motion for

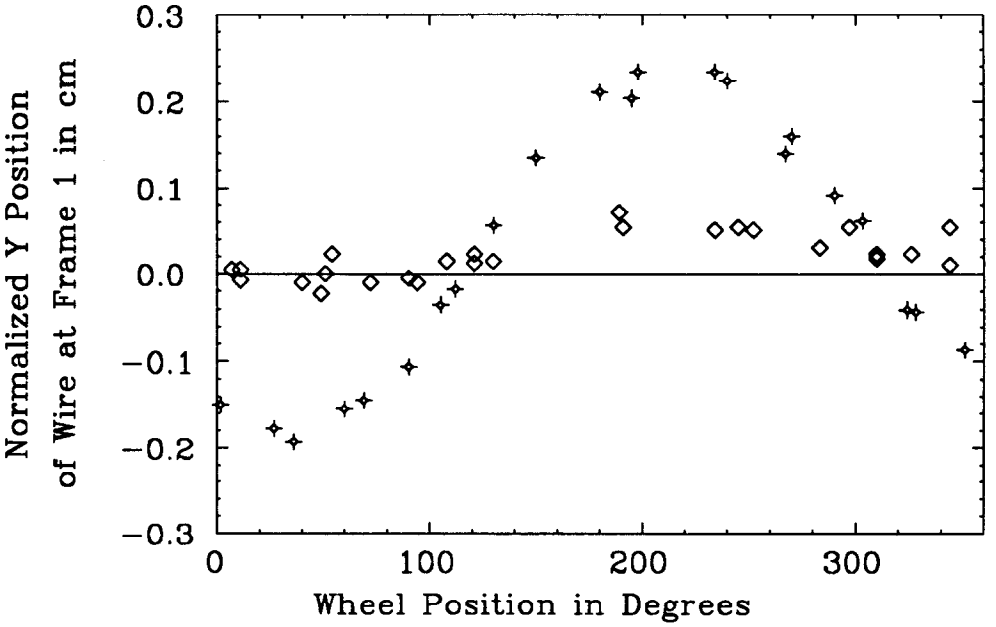

Figure 2.3. The pulley intrinsic torque. By maintaining a constant current in the wire and recording the y position of the wire at Frame 1, the induced tension could be mapped out as a function of wheel orientation. The crosses show the initial dependence and the diamonds the final dependence once the wheel was balanced with tape.

the system is given by:

$$\Theta = \frac{M}{K}\Big[\cosh(\sqrt{K}\,t) - 1\Big], \tag{2.2}$$

where

$$K = \frac{2r^2 g\rho}{I}\,, \quad \text{and} \quad M = \frac{gr(m_o + m_\tau)}{I}\,.$$

Here, Θ is the angle through which the pulley turns, r is the pulley radius, g is the acceleration due to gravity, ρ is the density of the wire supporting the two masses, I is the moment of inertia of the pulley wheel, and m_τ is the mass associated with the induced tension. One can solve for m_τ and m_o in terms of t_L, t_R, h_L, and h_R, where the subscripts L and R refer to the left and right sides of the pulley respectively. For

heights, h_L and h_R, both positive and measured in cm, this gives:

$$m_\tau = \rho \left[\frac{h_L}{\cosh(\sqrt{K}\, t_L) - 1} - \frac{h_R}{\cosh(\sqrt{K}\, t_R) - 1} \right] , \tag{2.3}$$

$$m_o = \rho \left[\frac{h_L}{\cosh(\sqrt{K}\, t_L) - 1} + \frac{h_R}{\cosh(\sqrt{K}\, t_R) - 1} \right] . \tag{2.4}$$

This technique was repeated for two values of m. In each case we found a slight sinusoidal dependence to m_τ on wheel orientation with an average value of -0.025 g $\pm$ 0.002 g. As a conservative estimate we assigned an overall systematic uncertainty of $\pm$ 0.020 g. Since the result was independent of m, the same correction was applied to data taken with both the 100 g and 410 g weights. Consistency between the results obtained with the two weights further indicated that this procedure was satisfactory. See for example, the forward coefficients, $\langle x_f | \theta_o \rangle$ and $\langle \theta_f | \theta_o \rangle$, and the plots of y_1 versus current in Appendix C.

2.1.2 Inner Frames

The inner frames provided precise and highly reproducible means of determining the wire position. Four inductors located on the inside of the cylindrical "position sensor", as shown in Figure 2.4, were sensitive to the EMF induced by a 25 kHz signal superimposed on the DC current in the wire. The two inductors on the **x** axis were coupled together and were used to determine the **x** position of the wire. Signals from these inductors were adjusted so that they were in phase, then amplified and subtracted from each other. The same was done for the two inductors on the **y** axis which were used to find the **y** position of the wire. The resultant signals were fed to an oscilloscope. The position sensors could be moved remotely in **x** and **y**. As the sensor was moved about the wire, the signals on the scope were observed to pass through a minimum and change phase. This minimum point was known as the "null" position of the wire and it indicated that the wire was centered electromagnetically

within the position sensor for the respective coordinate. When the "null" position was reached in both coordinates, the location of the position sensor, given by Sony Magnetic Strips, was recorded.

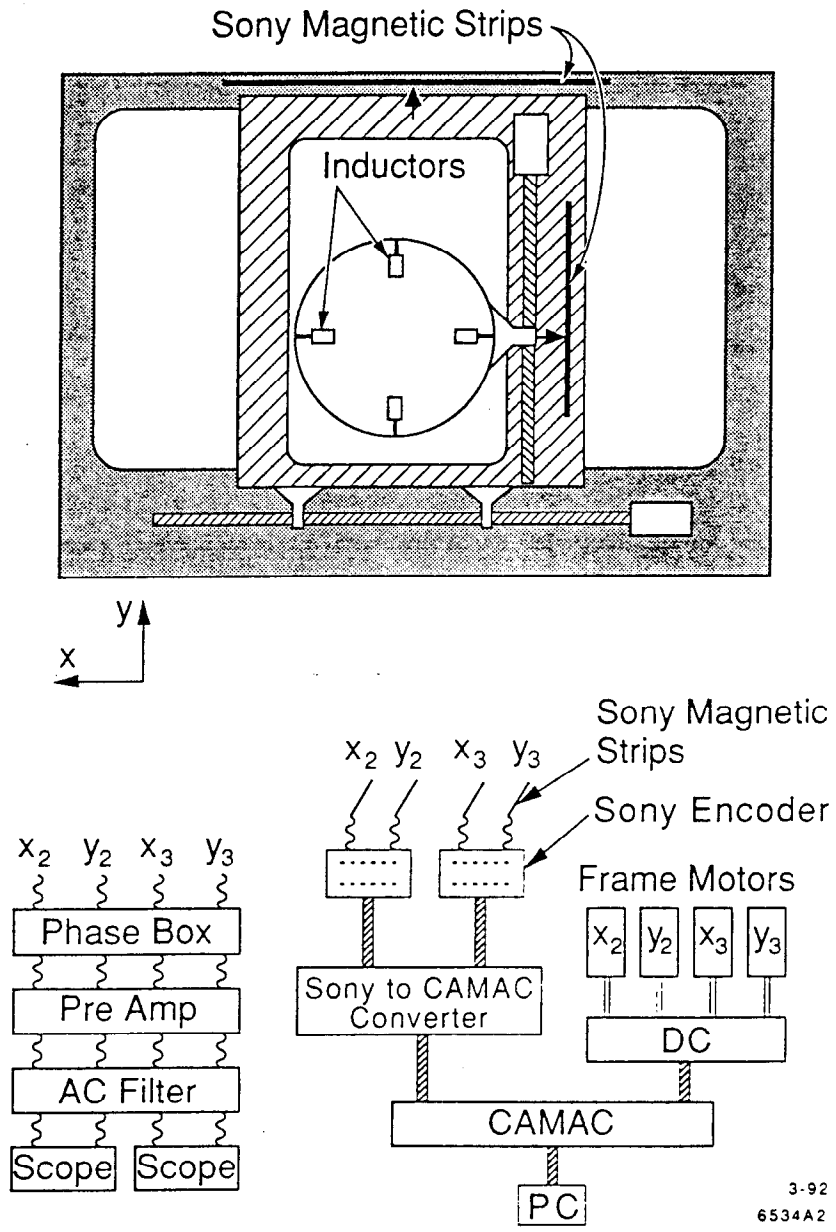

Figure 2.4. The inner frame position sensors. See text for a description.

The precision obtained with the inner frames was largely due to the automated process by which the inductors were centered around the wire and to the Sony mag-

netic strips which have a sensitivity rating of ± 0.00025 cm. Given an arbitrary floating wire, we were able to determine the **x** and **y** positions to within ± 0.0013 cm and ± 0.0025 cm respectively for Frame 2, and ± 0.0025cm and ± 0.0051 cm at Frame 3. These uncertainties doubled when the 100 g weight was used as the wire was slightly less stable due to high currents. Table 2.2 gives the uncertainties in determining the wire position at each frame. The statistical uncertainties are properties of the inner frames coupled with the electronics set–up. They correspond to uncertainties in the relative wire position, whereas the systematic uncertainties, which are much larger, stem from uncertainties in determining the absolute wire position from the survey. Appendix B describes the survey techniques and the origins of the survey uncertainties.

2.2 Uncertainties in the Measured Quantities

In this section the uncertainties in the tension, current, and position are summarized. Table 2.2 gives the value or range of values in each quantity and the corresponding statistical and systematic errors. The systematic uncertainties dominate, especially for the wire position. The total uncertainty in a given quantity is obtained by adding the systematic and statistical errors in quadrature.

2.2.1 Tension

The total tension† in the wire was given by the following relation:

$$T = M_T + m_\tau + m_\omega \ , \tag{2.5}$$

where M_T is the mass of the applied weight, m_τ is the mass associated with the tension due to friction in the air–bearing pulley, and m_ω is the mass of the length of wire running from the top of the pulley to the hanging weight. For a central ray m_ω

† Note for tension we use mass units. Thus tension has units of grams. The factor, g, for the acceleration due to gravity is contained in the constant in equation 1.13. The uncertainty for the local value of g is given in Table 2.2.

Table 2.2. A summary of the uncertainties. The x and y positions listed here represent displacements relative to the central trajectory at each of the respective frames. The quantities, $D_{1,2}$ and $D_{3,4}$ are the distances between frames 1 and 2 at the target and 3 and 4 in the hut respectively.

UNCERTAINTIES IN THE MEASURED QUANTITIES

Quantity	Value or Range of Values	Statistical Uncertainty (±)	Systematic Uncertainty (±)
Tension			
M_1	410.552 g	0.009 g	–
M_2	100.685 g	0.005 g	–
m_ω	0.054 g	–	0.005 g
m_τ	− 0.025 g	0.002 g	0.020 g
T_1	410.581 g	0.009 g	0.021 g
T_2	100.714 g	0.005 g	0.021 g
g	979.914 cm/sec^2	–	0.020 cm/sec^2
Current			
I	0.07 − 0.61 A	< 0.01%	0.017 − 0.022 %
Position * Double statistical error for 100 g weight			
x_1	± 10.2 cm	0.0076 cm	0.0076 cm
y_1	*Fixed* 0.0 cm	0.0076 cm	0.0178 cm
x_2	± 10.5 cm	0.0013* cm	0.0076 cm
y_2	± 4.6 cm	0.0025* cm	0.0178 cm
x_3	± 21.2 cm	0.0025* cm	0.0305 cm
y_3	± 12.5 cm	0.0051* cm	0.0508 cm
x_4	± 25.4 cm	0.0025 cm	0.0330 cm
y_4	± 10.1 cm	0.0025 cm	0.0483 cm
Frame Separations			
$D_{1,2}$	162.877 cm	0.0076 cm	0.635 cm
$D_{3,4}$	128.841 cm	0.0076 cm	0.640 cm

was estimated at 0.054 g ± 0.005 g. The dominant uncertainty in the tension comes from the intrinsic torque introduced by the air–bearing pulley. For the 100 g data, this amounted to a ± 0.02% uncertainty

2.2.2 Current

The current in the wire was determined by measuring the voltage drop over a 0.1 Ω shunt. The shunt and HP DVM were calibrated as a unit for currents ranging from 0.1 A to 1 A. The uncertainty in the calibration current was estimated at 0.01% at 0.1 A, or 0.00001 A. In addition to the uncertainty in the calibration current, we also included an uncertainty based on the observed fluctuations in the value of the current needed to get a level wire at 4 GeV. The standard deviation of the fluctuations was ±0.017% of the average value. An uncertainty of 0.017% was thus assigned for all currents at all momenta. The above two uncertainties were added in quadrature to give the total uncertainty in current listed in Table 2.2 The inclusion of an uncertainty due to the fluctuations in central current gives a conservative estimate of the total uncertainty since the observed fluctuations could also stem from true differences in the magnetic field settings. Without accurate magnetic field measurements (see section 3.1), we were unable to conclude the source of the observed fluctuations in current. The fit to the measured voltage versus calibration current yielded statistical uncertainties which were negligible.

2.2.3 Position

The uncertainties in the trajectory position measurements were dominated by systematic effects inherent in the survey method. For Frames 1 and 2, the systematic errors in x and y were due to the uncertainty in knowing the exact location of beam center–line and beam height. In the hut, since x and y were not measured directly, but rather determined from survey measurements of several other points, the systematic errors in wire positions at Frames 3 and 4 stemmed from errors in the measured hut quantities which were propagated through to the determination of x and y.

The most significant systematic uncertainty in position came from the measurement of the frame separations. This relatively large uncertainty was due to the design of the inner frames which made the location of the plane in which the wire position was sensored difficult to discern. Because the inductors were located within the cylindrical position sensor, it was difficult to measure them with a steel tape. Fortunately, this uncertainty limited the determination of the absolute acceptance and *not* the point–to–point or momentum dependence to the acceptance or matrix elements. It also had no affect on the central momentum calibration. It would be worthwhile to try and reduce this problem in future calibrations by marking the location of the plane on the exterior of the cylinder during assembly. The uncertainty in frame separation could be reduced by a factor of two before uncertainties in the other survey quantities would begin to dominate.

Statistical uncertainties in the inner frames give rise to the point–to–point fluctuations of the coefficients versus momentum. These uncertainties were small, 0.005 cm or less for the 410 g weight, and would be difficult to improve upon.

2.3 The Measurement Process and Data Sample

There were six data sets analyzed in this report and they are classified in Table 2.3. The data fall into one of two categories: those which pertain to the horizontal or production angle plane, where x and θ are varied; or those pertaining to the vertical or momentum dispersion plane where y, ϕ and δ are varied. Data sets 5 and 6 were taken with the 100 g weight while the others were taken with the 410 g weight. For each set the maximum possible range in momenta was covered. To go below 2 GeV with the 410 g weight, although the wire could support the current, introduced too much instability.

The measurement procedure was similar for all data sets. The spectrometer was set to the desired momentum according to a standard procedure. Whenever possible, and at least once per eight hour shift, a standard reference trajectory was floated at 4 GeV as a consistency check to ensure that the system was stable and

Table 2.3. Overview of the six data sets. Data set 6 and a subset of data set 4 were used to determine the central momentum. Data set 6 was insufficient to obtain first order optics coefficients since the range spanned by y_f was too small, *i.e.* near zero. This lack of data covering a larger range in y_f was due to a time constraint rather than any physical limitation.

THE DATA SAMPLE

Data Set	1	2	3	4	5	6
Tension	410 g	410 g	410 g	410 g	100 g	100 g
Momentum Range (GeV)	$2-9$	$3-9$	$2-9$	$2-9$	$0.5-4$	$0.5-4$
Average Number of Trajectories per $\vec{P}$ Setting	5	5	12	100	3	100
Order of Fit	1^{st}	1^{st}	2^{nd}	2^{nd}	1^{st}	–
Forward and/or Reverse Fit	*fwd*	*fwd*	*both*	*both*	*fwd*	*none*
Coefficients Yielded	x, θ	x, θ	x, θ	y, ϕ, δ	x, θ	*none*
Ranges spanned by variables						
x_o	0	0	± 10 cm	0	0	0
x_f	± 24 cm	± 30 cm	± 12 cm	0	± 24 cm	0
θ_o	± 5 mr	± 6 mr	± 3 mr	0	± 5 mr	0
θ_f	± 26 mr	± 32 mr	± 15 mr	0	± 26 mr	0
y_o	0	0	0	0	0	0
y_f	0	0	0	± 15 cm	0	± 5 cm
ϕ_o	0	0	0	± 28 mr	0	± 28 mr
ϕ_f	0	0	0	± 28 mr	0	± 28 mr
δ	0	0	0	± 5 %	0	± 2 %

reproducible. This was defined as a level wire entering the spectrometer on beam height, as determined via a transit on the floor, and exiting as close as possible† to the nominal spectrometer center line. The production angle data were taken with the wire endpoints fixed and the current adjusted such that the wire entered the spectrometer on beam height. When the wire was stable, the **x** and **y** coordinates at the four frames were recorded as well as the current. The endpoints were then changed and the process repeated until the desired range in x and θ was mapped out. In the vertical plane for each set of fixed endpoints approximately twenty-five trajectories were measured, each corresponding to a different δ, or current. For all measurements the **y** position of the target remained fixed at beam height consistent with the constraint that $y_o = 0$.

† Given the limitation of the grid hole spacings of Frame 4, the hole closest to beam center line actually corresponded to $x_4 = -0.54$ cm and $y_4 = -0.68$ cm.

3. Analysis and Results

The floating wire relation given by equation 1.13 is valid for a massless wire. To reconcile the fact that the measurements were made with a massive wire, a "mass correction" was needed, and applied to each trajectory. The mass correction provided a method for assigning a new trajectory to each measured one, such that the new trajectory corresponded to that which would have been measured had the wire truly been massless. Given the scale of the 8 GeV spectrometer, and hence the length of wire necessary to calibrate it, the size of the mass correction was large compared with the uncertainties in the measured quantities. Thus, it was important to fully study the mass–corrected data and provide careful checks to ensure the proper application of the correction. Appendix C describes the mass correction method and illustrates the checks which were used to demonstrate its accuracy.

Once each trajectory has been corrected for the mass of the wire, and its raw coordinates converted to TRANSPORT coordinates as described in Appendix B, the central momentum can be calibrated and the optics coefficients obtained via straight forward techniques. In addition, given the momentum dependence of the optics coefficients, one can draw some conclusions about the momentum dependence of the spectrometer acceptance. The techniques and results for the above are presented in the following sections. Also presented is a section pertaining to a new TRANSPORT model derived from a fit to this data and previously existing magnetic measurement and survey data. The model gives very good agreement with the data and has been used to generate a new standard set of reconstruction coefficients.

3.1 Central Momentum Calibration

The central momentum was measured for each of fourteen nominal momentum settings. For most set–points at least two measurements were made separated in

time by several days. To determine the central momentum, P_c, one needs to know the tension, T_c, and the current, I_c, which correspond to the central ray. A central ray is defined to be a ray which enters the spectrometer at beam height and on the spectrometer center line (see Appendix B) and exits at 30° to the horizontal. The tension† is given by equation 2.5. To obtain the central current, a quadratic fit to y_2 versus I for mass corrected trajectories was done for a subset of data sets 4 and 6 where $-2\% \leq \delta \leq 2\%$. The central current was then determined by evaluating I for $y_2 = 0$. This is equivalent to requiring the trajectory to enter the spectrometer at beam height. As a check, y_3 was also fit to a quadratic and the two values for central current agreed to 0.01%. With the central current determined, the central momentum is obtained from equation 1.13.

In Figure 3.1 the percentage deviation of the measured central momentum, P_c, from the nominal set point, P_o, is plotted for each measurement taken. The squares represent data taken with the 100 g weight, while the diamonds are data with the 410 g weight. The error bars contain the statistical error from the fit to I versus y_2, which is negligible, and the systematic error added in quadrature. The systematic error dominates and is perfectly correlated for all points. Thus, the error bars represent a uniform shift in the data rather than point–to–point fluctuations. The systematic errors were determined by adding in quadrature the uncertainties due to the tension, the current in the wire, and the determination of the local value for the acceleration due to gravity.

In looking at Figure 3.1, there are two points to note. The first concerns the peculiar shape of the curve, and the second is the apparent disparity in measurements particularly for $P_c \leq 4$ GeV. The shape of the curve stems from the polynomial which

---

† The tension on the wire changes as a function of δ due to the difference in length, and therefore mass, of the piece of wire running from the top of the pulley to the hanging mass, m_ω. However, the value for m_ω corresponds to the best estimate for a central ray where $\delta = 0$.

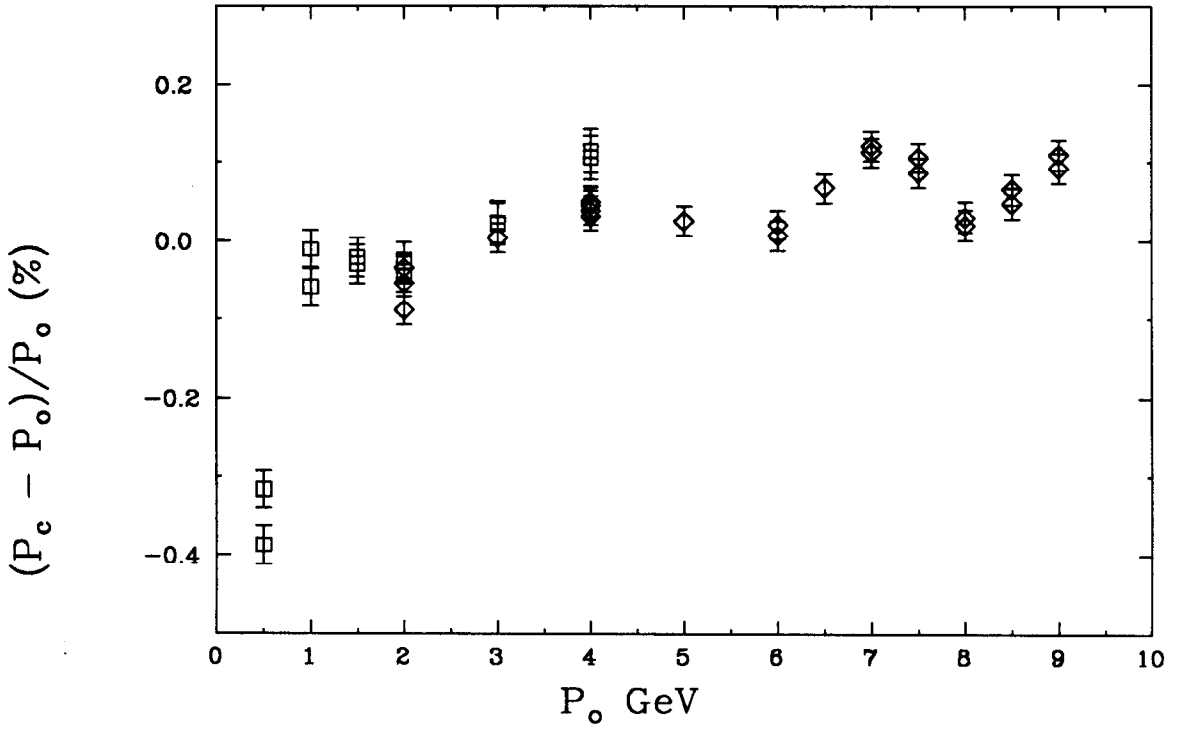

Figure 3.1. Deviations in P_c from the P_o. Shown are the percentage deviations of the measured central momentum, P_c, from the nominal momentum setting, P_o, of the spectrometer. The squares are 100 g data and the diamonds the 410 g data. The error bars are dominated by systematic uncertainties and are perfectly correlated for all points. They indicate a shift for all points rather than a point–to–point fluctuation in the measurement.

has historically been used to set the current in the dipoles. It is a five term polynomial† based on a fit to old data. Below 1 GeV the curve falls off since there was no data to constrain the fit in that region. (In recent experiments when data was taken below 1 GeV, a simple linear fit was used to set the dipoles for momenta below 1 GeV.) Thus, the shape of the curve is a direct result of the prescription used in setting

† The polynomial used during the wire float measurements is as follows:

$$a = -2.736 + (x)3.14 \times 10^{-2} - (x^2)8.491 \times 10^{-8} + (x^3)3.708 \times 10^{-12} - (x^4)7.139 \times 10^{-17} + (x^5)5.063 \times 10^{-22}.$$

Here $x = 8692\ P_o$ and the final current is given by $I = 1.0011\ a$.

the dipoles. The disparity in measurements made at the same set–point most likely corresponds to actual differences in the central momentum for a given nominal set–point. Unfortunately, field measurements were not taken each time the spectrometer was set to a different momentum, but rather at periodic intervals over the two months of data taking. It was later discovered that the current in the magnets was set to within $\pm$ 0.5 A. This uncertainty in current translates into an uncertainty in magnetic field of 0.004 kG, which is large enough to produce the observed differences in the central momentum measurements.

It is useful to fit the magnetic field versus momentum for future use. The values for P_c and B which were fit are given in Table 3.1. For each nominal set–point, an average was taken for the corresponding P_c measurements and the NMR[†] measurements which existed for that set–point. For the central momenta, the error bar on the averaged result, σP_c, was not reduced since it is dominated by systematic effects. However, the error bar on the resultant magnetic field, σB, was reduced accordingly, depending on the number of measurements, since it represents a statistical fluctuation. Before fitting P_c versus B, it was necessary to incorporate the error in B, the independent variable, into the error in P_c, the dependent variable. This was achieved by multiplying σB by the ratio of P_c/B, which is $\simeq 0.415$. This additional error in P_c, given in Table 3.1 by σP_c^B, was added in quadrature with σP_c to give the total error in P_c which was used in the fit.

The following equation was fit for momenta of 7.5 GeV or less to obtain the coefficients a_1 and a_2:

$$P_c = a_1 B + a_2, \tag{3.1}$$

where

$$a_1 \;=\; 0.41511 \pm 0.00006 \;\; (\mathrm{GeV/kG}),$$

[†] The magnetic fields given in Table 3.1 correspond to magnet B81. The fields in B82 were normalized to those in B81 in order to correct for an offset found during the analysis which caused the fields in B82 to be set 1% low at 0.5 GeV. The data were corrected for this effect.

Table 3.1. The 8 GeV spectrometer characteristics. Given are the measured values of the central momentum, P_c, the dipole magnetic fields, B, and their respective uncertainties. σP_c is the error in measuring P_c, while σP_c^B is the additional error in P_c which comes from the uncertainty in magnetic field, σB.

8 GeV FIELDS AND MOMENTA

P_o (GeV)	P_c (GeV)	σP_c (±GeV)	B (kG)	σB (±kG)	σP_c^B (±GeV)
Data taken with the 410 g weight					
2.0	1.99899	0.00036	4.8160	0.0017	0.00070
3.0	3.00012	0.00054	7.2271	0.0023	0.00095
4.0	4.00172	0.00073	9.6402	0.0028	0.00116
5.0	5.00128	0.00092	12.0458	0.0040	0.00166
6.0	6.00065	0.00111	14.4538	0.0023	0.00095
6.5	6.50435	0.00121	15.6640	0.0040	0.00166
7.0	7.00805	0.00132	16.8824	0.0028	0.00116
7.5	7.50786	0.00141	18.0842	0.0028	0.00116
8.0	8.00198	0.00152	19.2820	0.0028	0.00116
8.5	8.50482	0.00163	20.4923	0.0028	0.00116
9.0	9.00937	0.00174	21.7128	0.0028	0.00116
Data taken with the 100 g weight					
0.5	0.49824	0.00012	1.1976	0.0013	0.00054
1.0	0.99974	0.00024	2.4072	0.0015	0.00062
1.5	1.49959	0.00038	3.6119	0.0018	0.00075
2.0	1.99922	0.00051	4.8160	0.0017	0.00070
3.0	3.00069	0.00079	7.2271	0.0023	0.00095
4.0	4.00442	0.00112	9.6402	0.0028	0.00116

$$a_2 = 0.00054 \pm 0.00042 \ \text{(GeV)},$$

and the off-diagonal element of the covariance matrix is $\sigma^2_{a_1,a_2} = -1.92 \times 10^{-8}$. This fit is very useful as it allows the central momentum to be calculated from NMR measurements of the dipoles. With new, highly accurate NMR probes installed in 1988, P_c can be determined to an accuracy of ± 0.07% at 0.5 GeV and 0.01% at 8

GeV. This was used in SLAC experiment NE11. Figure 3.2 illustrates the deviation of the measured values of P_c from the fitted value, P_{fit}. The error bars on the low momentum points are dominated by the large statistical uncertainty in knowing the value of the magnetic field for each measurement. The 100 g and 410 g data are plotted with the solid and open diamonds respectively. The level of agreement between the two data sets is an indication of the accuracy of the mass correction.

We can conclude that the central momentum was measured to $\pm 0.02\%$ for momenta greater than or equal to 2 GeV, and to $\pm 0.025\%$ for momenta less than 2 GeV. This precision is a statement of the accuracy obtained using the floating wire technique, namely of measuring the central momentum via the floating wire relation, equation 1.13. However, since measurements of the dipole fields were not made with equivalent precision, it is their uncertainties which limit the precision with which the central momentum can be determined via NMR measurements in the future.

3.2 Optics Coefficients

The optics coefficients were obtained from linear fits to the initial and final coordinate vectors, Equations 1.7 and 1.8. To determine δ we made use of our knowledge of the central current, I_c, as defined above for the central momentum calibration. We can write δ as follows:

$$\delta = \frac{(I_c - I)}{I}, \tag{3.2}$$

where I corresponds to the current in an arbitrary trajectory. A factor, T/T_c multiplying I_c has been neglected since it was negligible in our case. The fits were either first–order or second–order linear polynomial depending on the number of trajectories in a given data set. Table 2.3 summarizes the order of the fit used for each data set, and which coefficients were determined. The fits also gave a constant offset term. Due to the nature of the data, namely that either x or y was varied but never both simultaneously, the horizontal and vertical planes of the spectrometer were treated independently. To first–order the horizontal and vertical focusing properties are independent, so this is a valid approximation. As a consequence however, cross terms

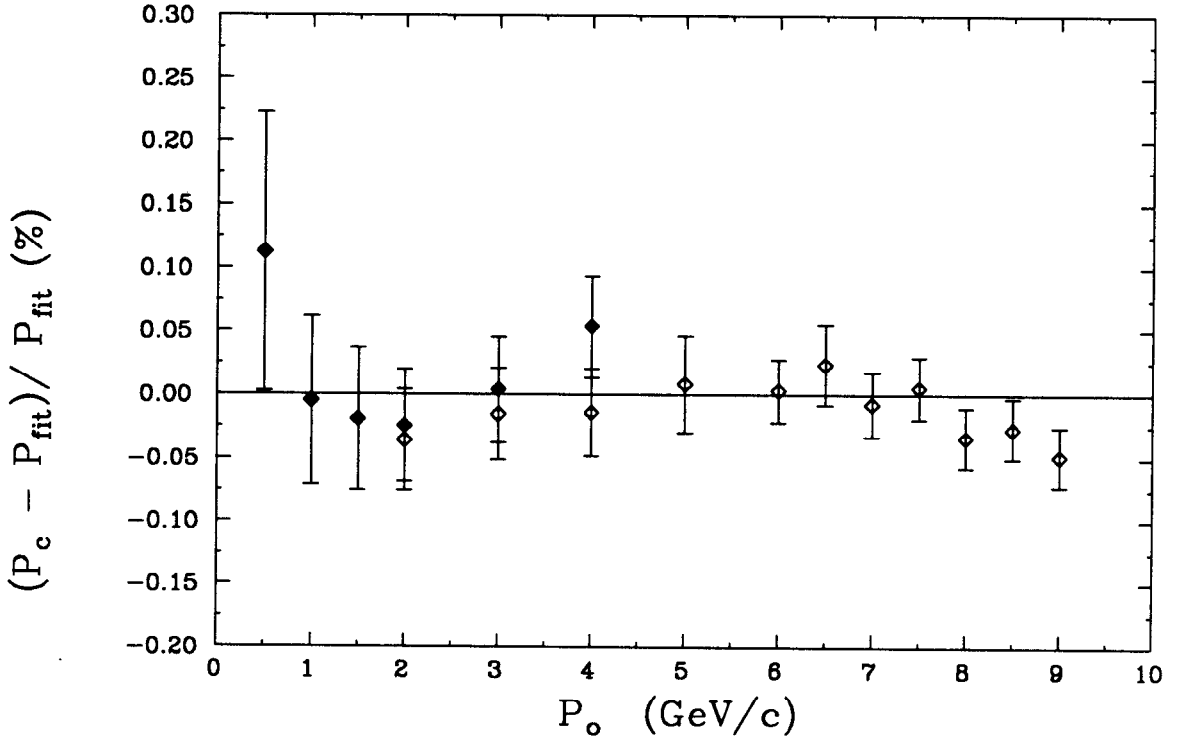

Figure 3.2. Deviations in P_c from the fitted value, P_{fit}. The solid diamonds are 100 g data and the open diamonds the 410 g data. The error bars for the low momentum points are dominated by the uncertainty in the magnetic field.

between the two planes were not obtained.

3.2.1 Statistical Uncertainties

The statistical uncertainties in the coefficients were due to random fluctuations in the data sample consistent with the uncertainties in measuring the coordinates of each trajectory at the inner frames. It is important to note that only the statistical uncertainties associated with the inner frame position measurements led to statistical uncertainties in the coefficients. The statistical errors in determining the coordinates at the outer two frames were propagated systematically since for a given data set they affected every trajectory in the same way. In other words, they did not introduce random fluctuations in the data. A similar argument holds for the statistical uncertainty in the tension, as listed in Table 2.2. It was propagated systematically

throughout the data analysis.

To determine the statistical errors on the coefficients, a Monte Carlo simulation was used. This was needed since the fitting routine did not allow each element in the coordinate vector to be weighted differently, and there was no means of weighting the independent variables. The Monte Carlo method consisted of fitting the data ten thousand times, each time randomly varying the coordinates of the inner frames via a Gaussian distribution centered about the nominal measured values, with a width corresponding to the uncertainty in the wire position coordinates. The results gave a spread in values about the nominal for each coefficient, and the quoted statistical error was taken to be plus or minus the half–width half–maximum value. The Monte Carlo was run for a single momentum for the 410 g weight and the 100 g weight since the errors in the wire position depended only on which tension was used and not on the momentum of the spectrometer.

3.2.2 Systematic Uncertainties

The systematic uncertainties in the fitted coefficients, or any derived quantity, were obtained by taking the square root of the sum of the squares of the deviations in that quantity caused by propagating the uncertainty associated with each "raw" measurement through the analysis procedure. In other words, if we let V_j represent a quantity whose error we wish to determine, for example a particular coefficient, then σV_j is given by:

$$\sigma V_j = \left[\sum_i v_{ij}^2 \right]^{\frac{1}{2}}, \tag{3.3}$$

where v_{ij} is the deviation in V_j caused by propagating the i^{th} uncertainty through the analysis. This method assumes the uncertainties to be uncorrelated errors, and this was the case. There were approximately seventy uncertainties, corresponding to each individual survey measurement, the tension, and the current. This method was used to arrive at the systematic uncertainties listed in Table 2.2 for the x and y positions in the hut frames since these positions were derived from the survey measurements.

3.2.3 *Forward and Reconstruction Coefficients*

Figures 3.3–3.11 contain plots of the momentum dependence of the non–zero forward and reconstruction optics coefficients. Previous data are plotted for comparison unless they are sufficiently off scale. In addition, model curves, which will be described in the following section, are plotted for all coefficients except the offsets. One should note that there is no data below 3 GeV for the vertical plane coefficients[†] and none below 2 GeV for the reverse horizontal plane coefficients. This was due to a lack of data taken with the 100 g weight which resulted from a time constraint. The solid diamonds are wire float data, the open circle is the jailbar point, and the open diamonds correspond to the 1968 dark–current beam data. The error bars on the wire float points are statistical and show the point–to–point fluctuations versus momentum. The systematic error is indicated by the error bar to the left of the first point. It is the same for all points and is perfectly correlated. Thus, it reflects a shift in the magnitude of the data rather than a change in shape, or momentum dependence of the coefficients. For the previous data points, the cross hatch on the error bars gives the statistical uncertainty and the extended error bar is the total error, statistical and systematic added in quadrature. The systematic uncertainties were ascribed to the previous data points in the following manner: $\pm$ 1% for the well–measured, large first order coefficients; a value equal to the systematic error obtained in the wire float for all other coefficients as a lower bound estimate.

An important feature of these plots is the momentum dependence observed in many of the coefficients. Although not nearly as severe as the previous measurements indicated, particularly for the momentum dispersion, $\langle y_f|\delta\rangle$, this dependence must be incorporated into the analysis of precision experiments. More will be said about the momentum dependence of the optics coefficients in the next section.

[†] The 2 GeV data was disregarded as it is suspected that a faulty hysteresis curve was followed in setting the magnets.

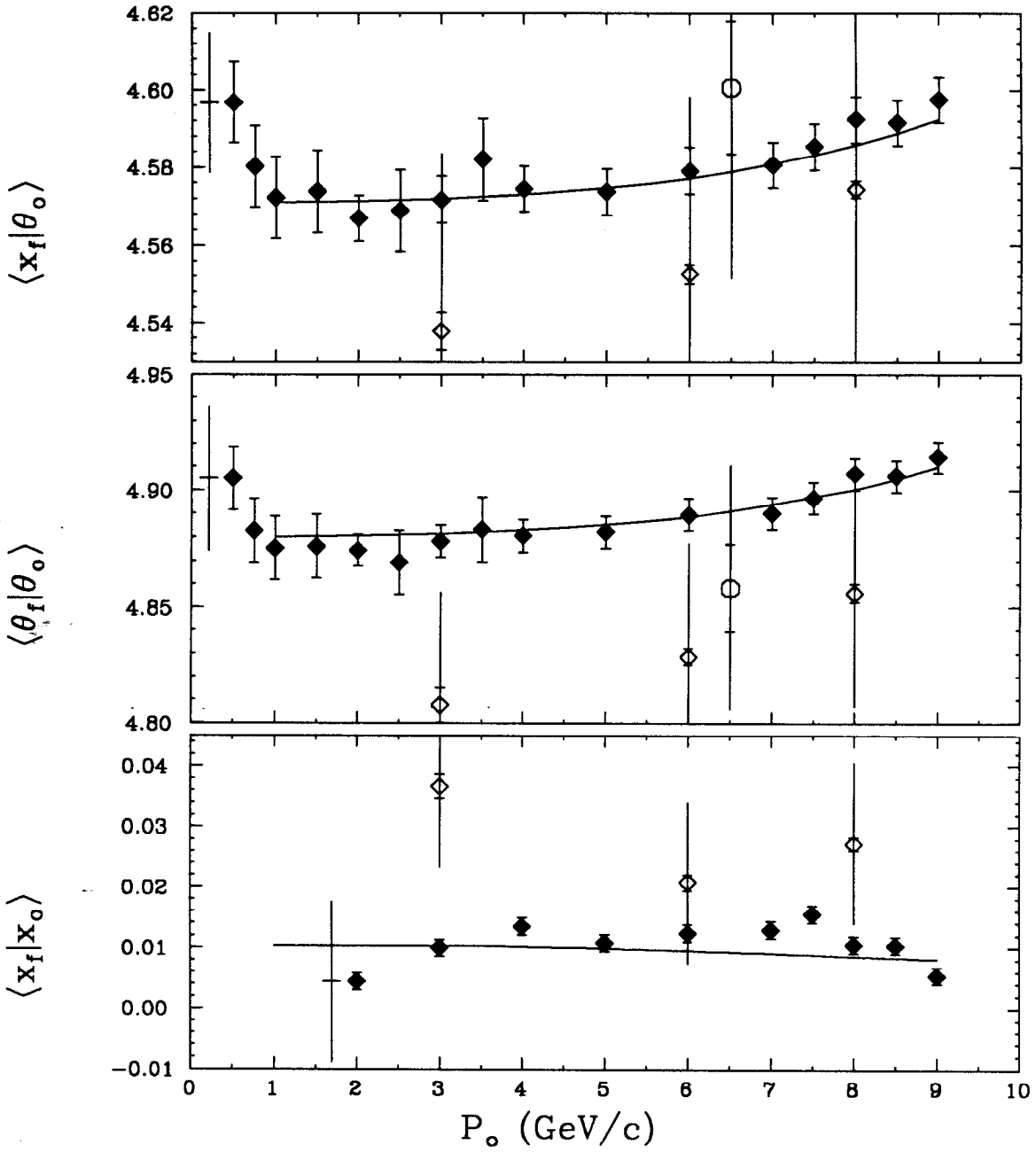

Figure 3.3. Forward coefficients measured in the wire float. The solid diamonds are wire float data, the open diamonds are 1968 dark–current data, and the open circle is the jailbar point. The solid curve is from a new TRANSPORT model constrained by the measurements. The error bars on the wire float data are statistical only. The bar to the left of the first point gives the systematic error which is the same for all points and perfectly correlated. See the text for errors on the 1968 and jailbar points.

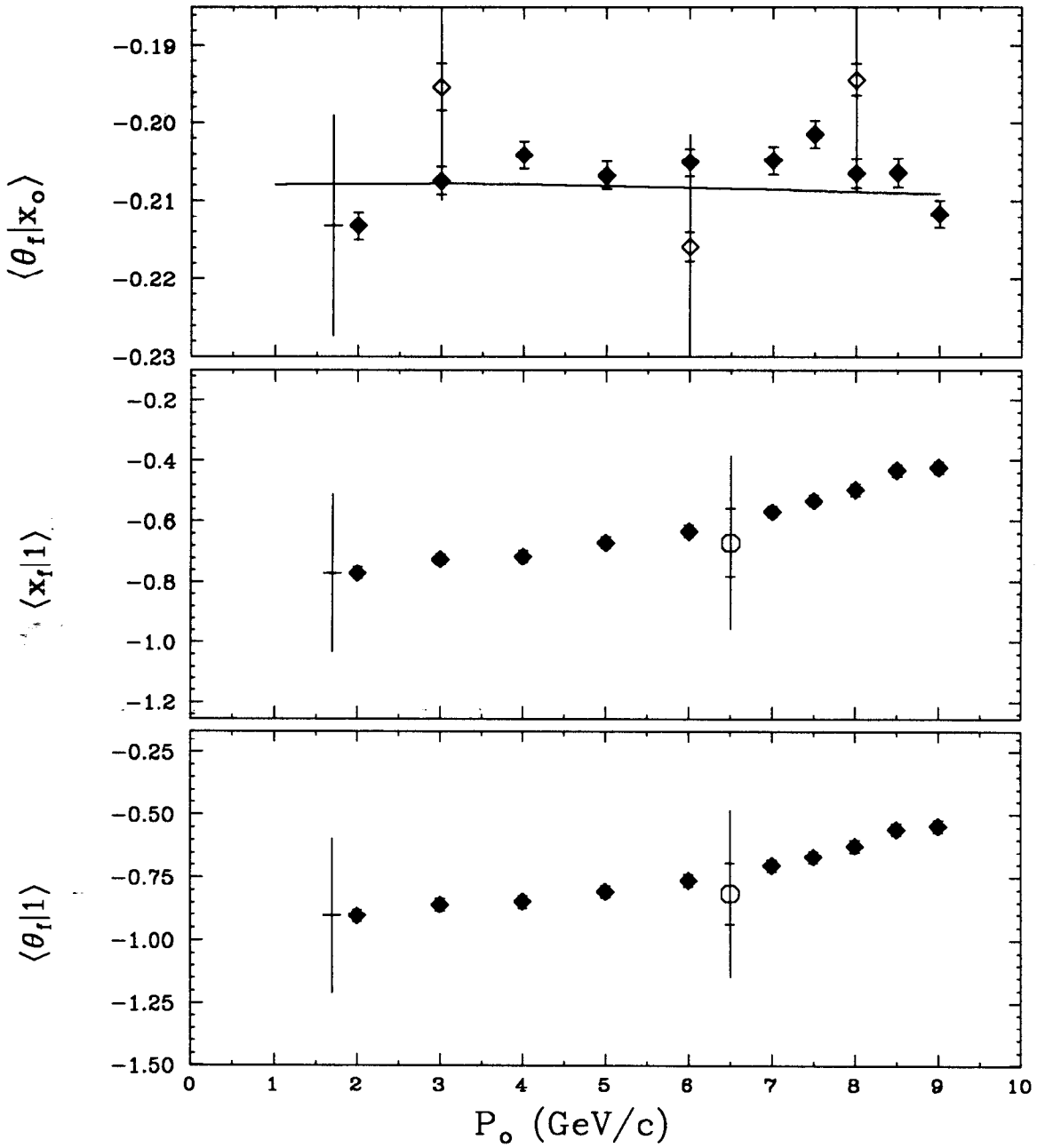

Figure 3.4. Forward coefficients measured in the wire float. The solid diamonds are wire float data, the open diamonds are 1968 dark–current data, and the open circle is the jailbar point. The solid curve is from a new TRANSPORT model constrained by the measurements. The error bars on the wire float data are statistical only. The bar to the left of the first point gives the systematic error which is the same for all points and perfectly correlated. See the text for errors on the 1968 and jailbar points.

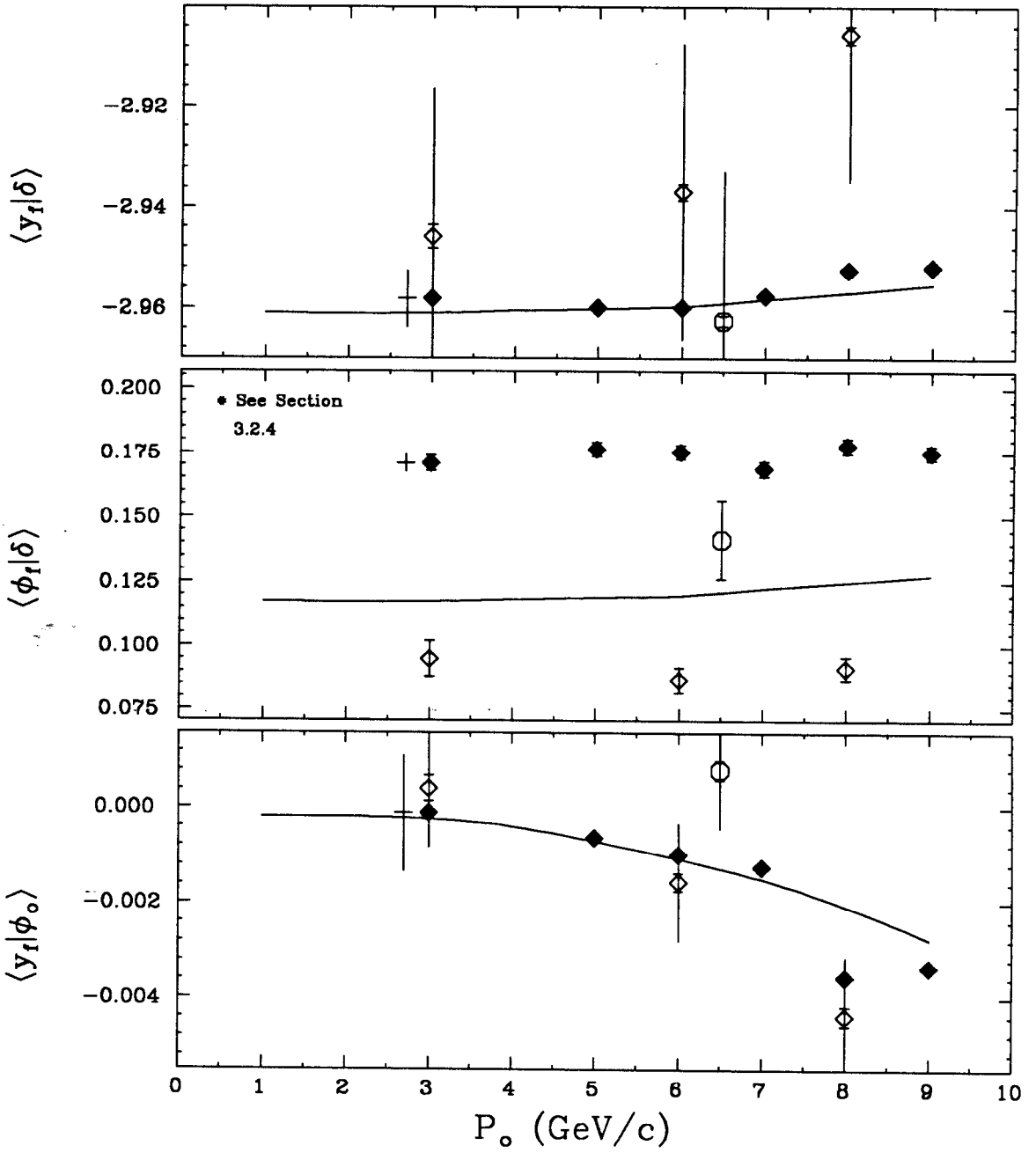

Figure 3.5. Forward coefficients measured in the wire float. The solid diamonds are wire float data, the open diamonds are 1968 dark-current data, and the open circle is the jailbar point. The solid curve is from a new TRANSPORT model constrained by the measurements. The error bars on the wire float data are statistical only. The bar to the left of the first point gives the systematic error which is the same for all points and perfectly correlated. See the text for errors on the 1968 and jailbar points.

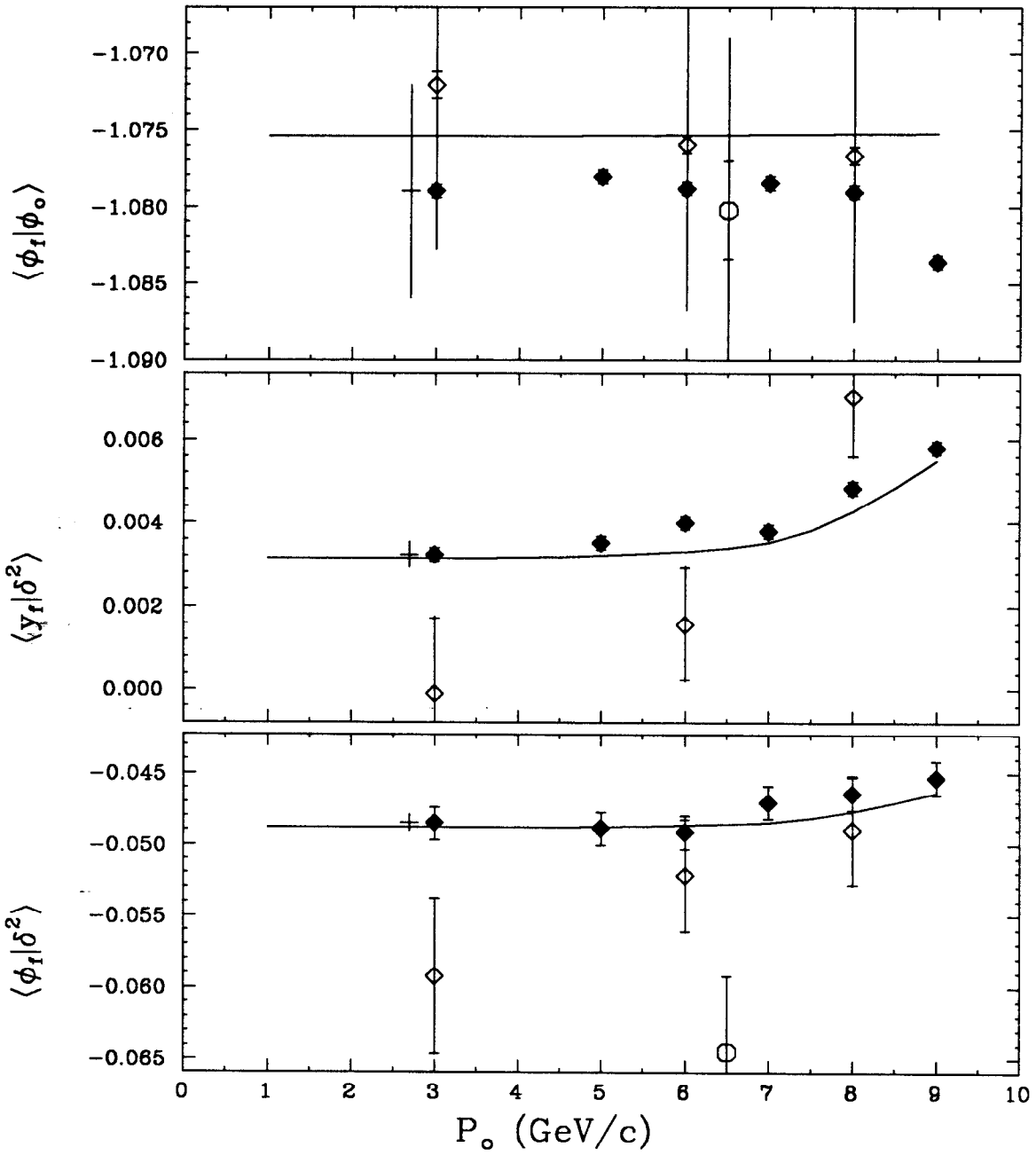

Figure 3.6. Forward coefficients measured in the wire float. The solid diamonds are wire float data, the open diamonds are 1968 dark–current data, and the open circle is the jailbar point. The solid curve is from a new TRANSPORT model constrained by the measurements. The error bars on the wire float data are statistical only. The bar to the left of the first point gives the systematic error which is the same for all points and perfectly correlated. See the text for errors on the 1968 and jailbar points.

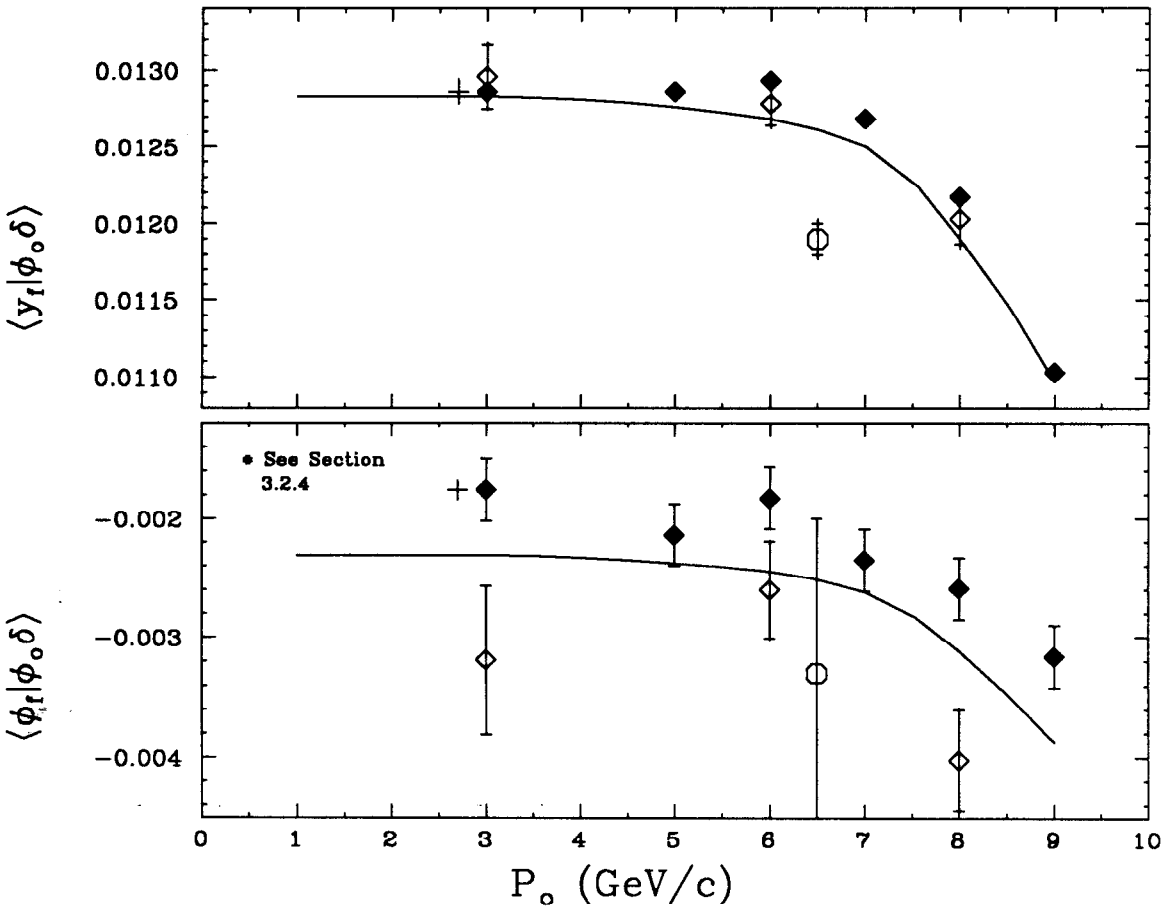

Figure 3.7. Forward coefficients measured in the wire float. The solid diamonds are wire float data, the open diamonds are 1968 dark–current data, and the open circle is the jailbar point. The solid curve is from a new TRANSPORT model constrained by the measurements. The error bars on the wire float data are statistical only. The bar to the left of the first point gives the systematic error which is the same for all points and perfectly correlated. See the text for errors on the 1968 and jailbar points.

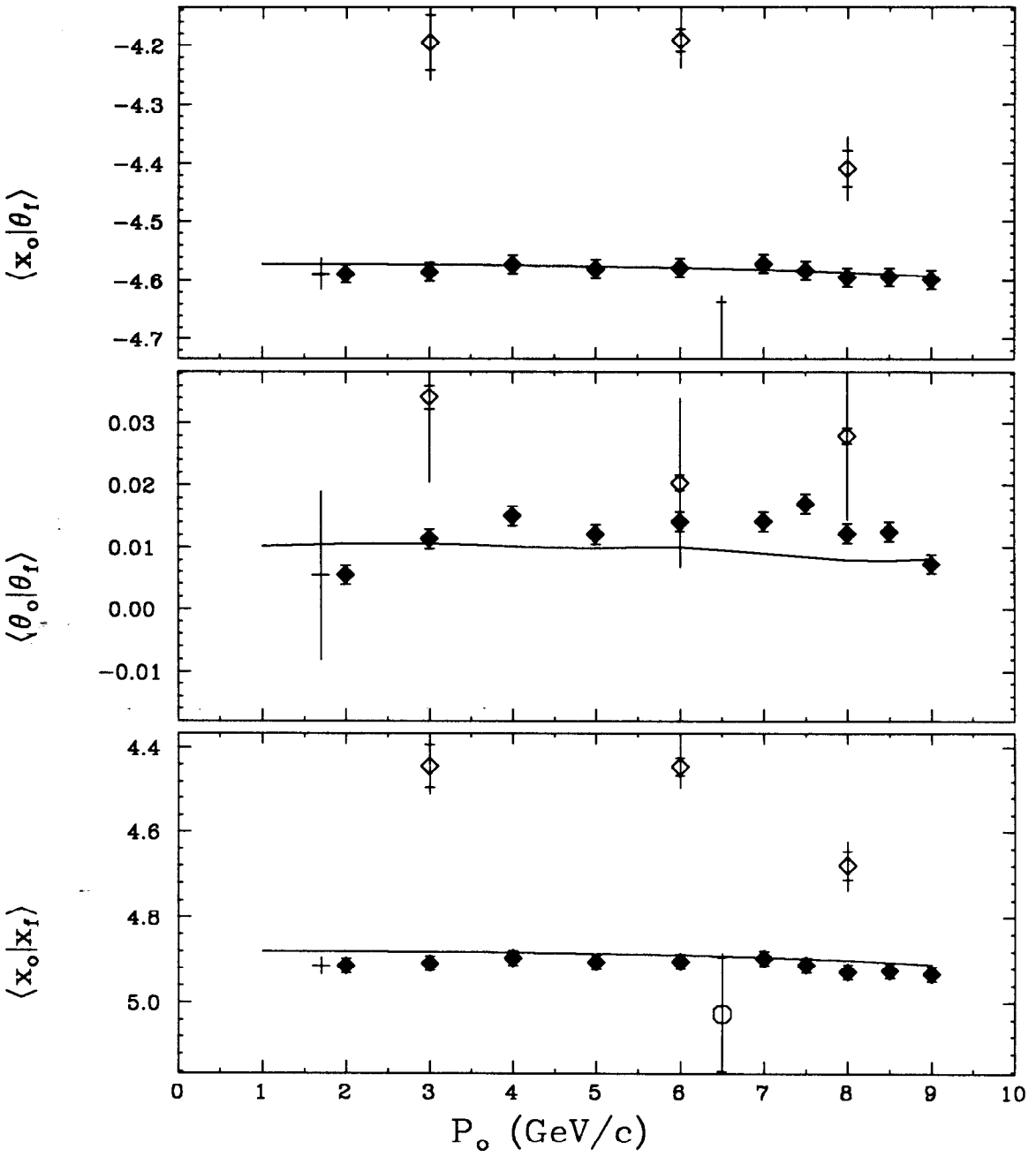

Figure 3.8. Reconstruction coefficients measured in the wire float. The solid diamonds are wire float data, the open diamonds are 1968 dark-current data, and the open circle is the jailbar point. The solid curve is from a new TRANSPORT model constrained by the measurements. The error bars on the wire float data are statistical only. The bar to the left of the first point gives the systematic error which is the same for all points and perfectly correlated. See the text for errors on the 1968 and jailbar points.

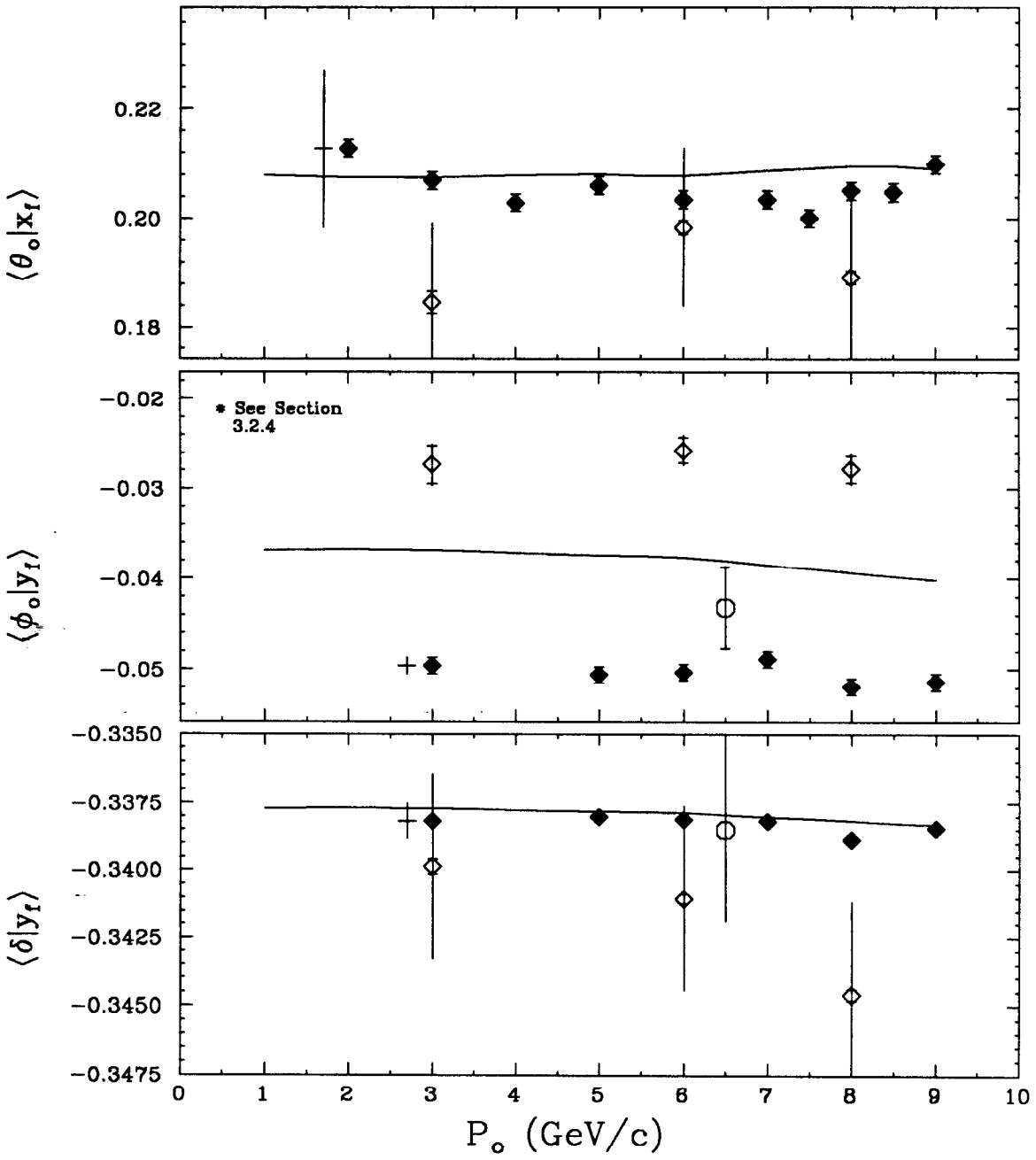

Figure 3.9. Reconstruction coefficients measured in the wire float. The solid diamonds are wire float data, the open diamonds are 1968 dark-current data, and the open circle is the jailbar point. The solid curve is from a new TRANSPORT model constrained by the measurements. The error bars on the wire float data are statistical only. The bar to the left of the first point gives the systematic error which is the same for all points and perfectly correlated. See the text for errors on the 1968 and jailbar points.

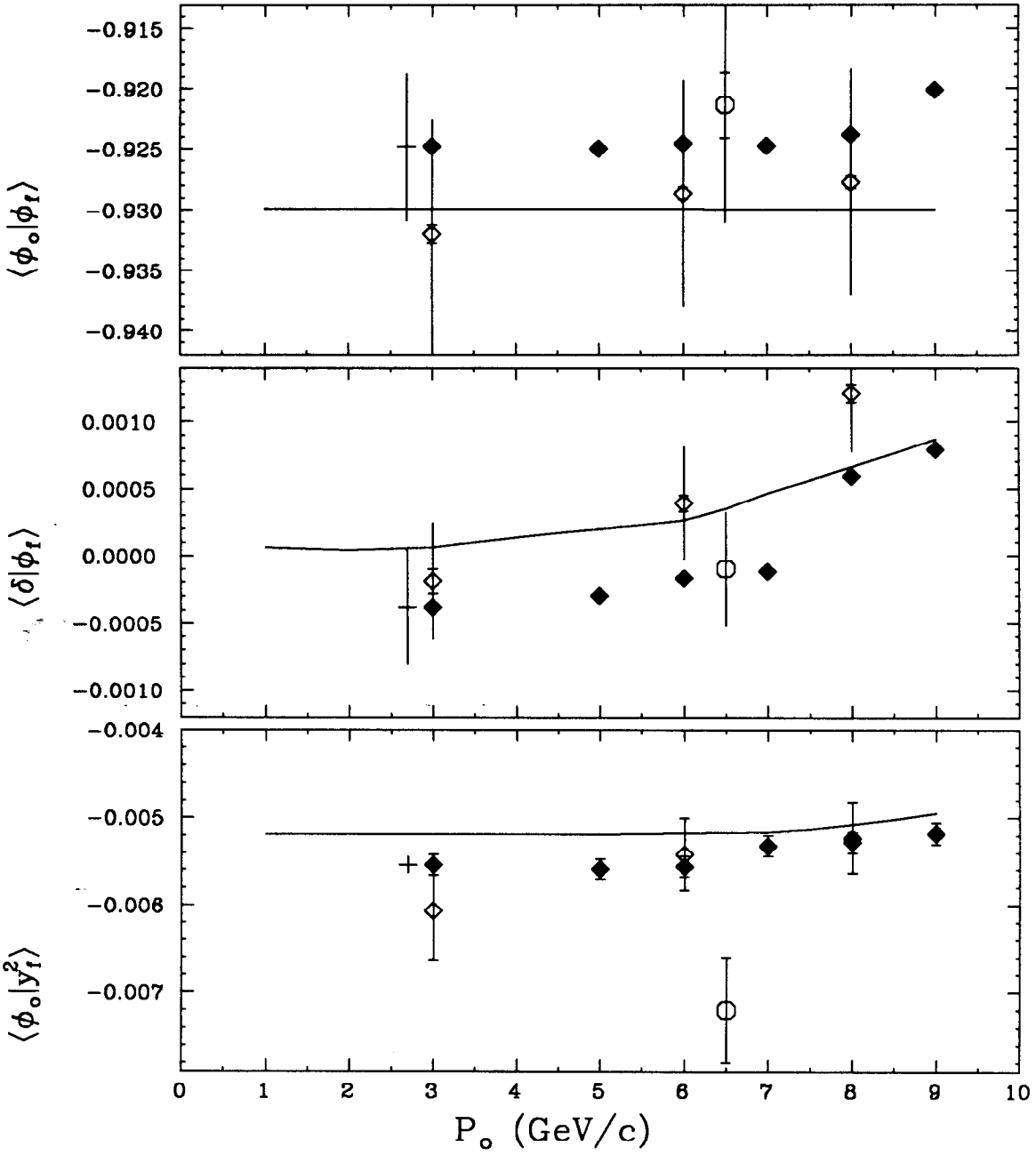

Figure 3.10. Reconstruction coefficients measured in the wire float. The solid diamonds are wire float data, the open diamonds are 1968 dark–current data, and the open circle is the jailbar point. The solid curve is from a new TRANSPORT model constrained by the measurements. The error bars on the wire float data are statistical only. The bar to the left of the first point gives the systematic error which is the same for all points and perfectly correlated. See the text for errors on the 1968 and jailbar points.

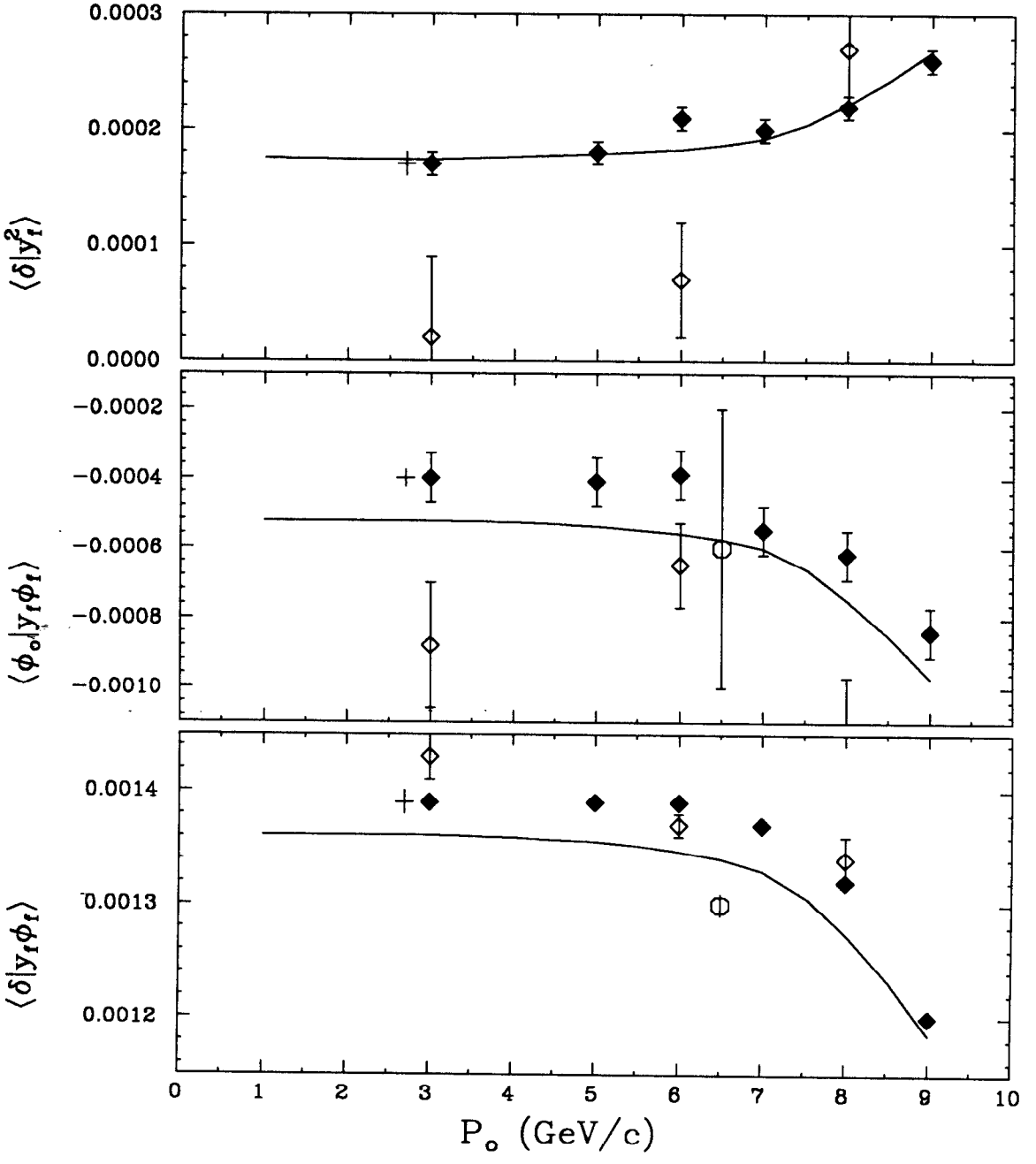

Figure 3.11. Reconstruction coefficients measured in the wire float. The solid diamonds are wire float data, the open diamonds are 1968 dark-current data, and the open circle is the jailbar point. The solid curve is from a new TRANSPORT model constrained by the measurements. The error bars on the wire float data are statistical only. The bar to the left of the first point gives the systematic error which is the same for all points and perfectly correlated. See the text for errors on the 1968 and jailbar points.

3.2.4 Modeling the Data

A new TRANSPORT model was developed based on the wire float optics measurements and a series of magnetic[17] and survey[18] measurements of the dipoles and quadrupoles. The model is able to reproduce the optics coefficients and their observed momentum dependence, illustrated in figures 3.3–3.11, by incorporating a momentum dependence to certain parameters which mimic effects due to saturation and variation of quadrupole focusing strength with momentum. The model used magnetic measurements and survey data to set the initial field strengths and drift distances. It also took into account the asymmetric positions of the quadrupole mirror plates which introduced an effective z offset in the quadrupole magnetic center with respect to the mechanical centers. The product of the quadrupole field gradient times the effective length was varied, within an estimated maximum uncertainty of 0.5%, until the model reproduced the measured optics coefficients at 3 GeV. Table 3.2 gives the new TRANSPORT model for 3 GeV. The final values for the product of the quadrupole field gradient times effective length are in good agreement with the average measured values obtained from magnetic measurements. The agreement is within 0.3%, 0.1% and 0.5% for Q81, Q82, and Q83, respectively.

There are three effects which give rise to the momentum dependence of the coefficients, and can be incorporated into the model by varying the TRANSPORT parameters given in Table 3.3 and described below. The first effect is due to the saturation of the dipoles at high fields. This effect changes the shape of the fringe fields and thus the focusing of the pole face rotations. It can be modeled by the TRANSPORT parameter K_1, and affects the first–order non–bend plane coefficients. It is responsible for half the slope observed in the $\langle x_f|\theta_o\rangle$ and $\langle\theta_f|\theta_o\rangle$ coefficients. The second effect comes from the fact that the integrated field, $\int B \cdot dl$, versus y in the dipoles depends on the magnet current. This effect is modeled by varying the radii of curvatures of the entrance and exit faces of the dipoles, $R_{1,2}$, and causes the momentum dependence observed in the second–order vertical plane coefficients. The third effect, unlike the first two which are consistent with the magnetic measurements and are physical prop-

Table 3.2. A new TRANSPORT model of the 8 GeV. This table contains the input file for an updated TRANSPORT model based on the measured optics coefficients, survey and magnetic measurements.

A NEW TRANSPORT MODEL FOR THE 8 GeV SPECTROMETER

1	'BEAM'	1.0	1.0	1.0	1.0	0.	0.	3.000;
17.	'2ND '				;			
16. 5.	'HGAP'				17.50 ;			
16. 7.	'KPAR'				0.518 ;			
16. 12.	'IRAD'				0.000 ;			
16. 13.	'ORAD'				0.000 ;			
3.0	'DRFT'				2.3181 ;			
5.0	'Q81 '			1.0369	2.8467	13.97 ;		
3.0	'DRFT'				0.9257 ;			
5.0	'Q82 '			1.3385	−4.0815	19.37 ;		
3.0	'DRFT'				0.9748 ;			
20.	'DROT'				−90. ;			
2.0	'PFRO'				7.50 ;			
4.0	'B81 '			3.6183	7.2404	0.0 ;		
2.0	'PFRO'				7.50 ;			
20.	'DROT'				90. ;			
3.0	'DRFT'				0.9385 ;			
20.	'DROT'				−90. ;			
2.0	'PFRO'				7.50 ;			
4.0	'B82 '			3.6183	7.2404	0.0 ;		
2.0	'PFRO'				7.50 ;			
20.	'DROT'				90. ;			
3.0	'DRFT'				1.0137 ;			
5.0	'Q83 '			1.3385	−2.6874	19.37 ;		
3.0	'DRFT'				4.7333 ;			
13. 4.	'PRNT'				;			
SENTINEL								

erties of the dipoles, comes from an incorrect momentum dependent correction which is used to set the current in the quadrupoles. The current is set linearly versus momentum, but there is an additional momentum dependent term for momenta of 4.5 GeV and above. This additional term, established in the 1968 dark–current calibra-

tion, effectively changes the quadrupole focal lengths. To reproduce this effect in the model, the quadrupole field gradients are varied for momenta of 4 GeV and greater. This effect is responsible for half the slope found in the $\langle x_f|\theta_o\rangle$ and $\langle\theta_f|\theta_o\rangle$ coefficients, and all of the momentum dependence observed in the vertical plane coefficients.

Table 3.3. Momentum dependence of TRANSPORT parameters. Here R_1 and R_2 are the radii of curvature of the entrance and exit faces of the dipoles, respectively. They are given in the TRANSPORT model by the codes 16. 12 and 16. 13. K_1 is a parameter which characterizes the extent of the fringing field of a bending magnet, given by a code of 16. 7. $\frac{G(P_o)/P_o}{G(3)/3}$ is the ratio of quadrupole field gradients for a momentum P_o relative to 3 GeV. These numbers multiply the quadrupole field gradients given above at 3 GeV to determine the gradient for a given momentum.

VARIATION OF
TRANSPORT PARAMETERS

P_o	$\frac{1}{R_1}, \frac{1}{R_2}$	K_1	$\frac{G(P_o)/P_o}{G(3)/3}$
1.0	0.0	0.511	1.0
3.0	0.0	0.518	1.0
4.0	−0.002	0.523	1.00017
5.0	−0.008	0.533	1.00034
6.0	−0.018	0.547	1.0005
7.0	−0.040	0.564	1.0010
8.0	−0.114	0.590	1.0015
9.0	−0.228	0.630	1.0020

Figure 3.12 shows a raytrace with respect to the central trajectory of the horizontal and vertical planes of the spectrometer using the new TRANSPORT model. The dashed line represents the respective focal planes. Note that the theta focal plane is now a few cm downstream of the momentum focal plane, whereas the 1968 beam data placed it approximately a half meter upstream of the momentum focal plane. The rays which end abruptly are lost due to apertures.

Excellent agreement can be found between the model and the measurements for

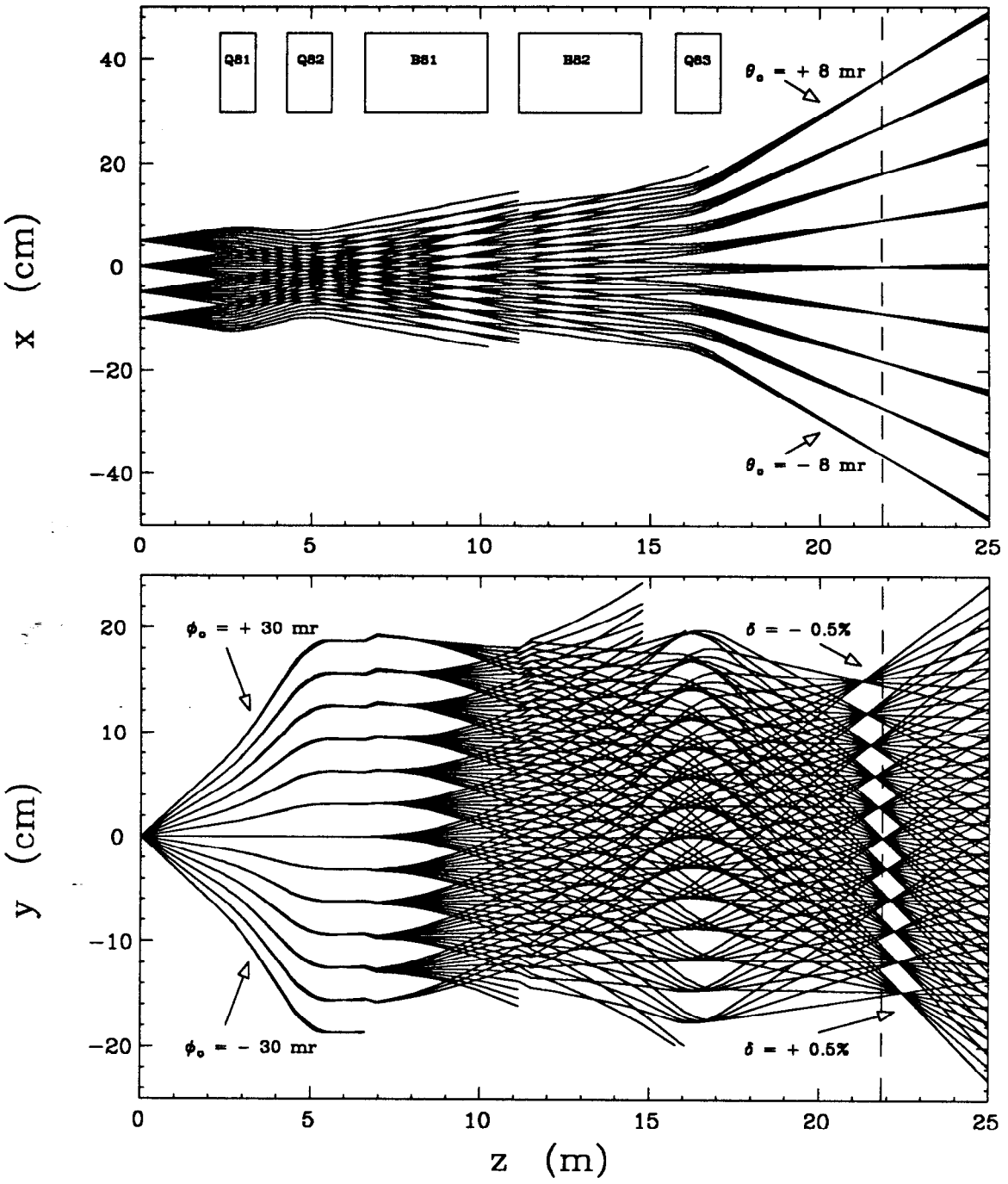

Figure 3.12. Raytrace of 8 GeV using the new TRANSPORT model. The horizontal, or theta plane is shown in the upper plot, while the vertical, or momentum dispersion plane is given in the lower plot. The location of the magnets in z is marked accordingly. The dashed line refers to the respective focal planes. Note that the momentum focal plane is tilted forward due to chromatic aberrations, and that the two focal planes are located nearly at the same point. Rays ending abruptly are lost due to apertures.

most forward coefficients, with the exception of $\langle \phi_f | \delta \rangle$ and $\langle \phi_f | \phi_o \delta \rangle$. Both of these coefficients are heavily dependent on the order of the fitting function. The TRANSPORT model corresponds to an exact second order fit. It can be shown that a third order fit to the data will yield values for these coefficients which are in better agreement with those obtained in the TRANSPORT model. A similar argument holds for the reverse optics. The reverse model curves were generated by running TRANSPORT with the elements in the reverse order and then applying the equations and coordinate rotations described in Appendix A. Note that TRANSPORT does not yield constant offsets, however those measured in the wire float, $\langle x_f | 1 \rangle$, and $\langle \theta_f | 1 \rangle$, are real, and most likely due to slight misalignment of the quadrupoles. However, since the spectrometer has been dismantled after NE11, there is no reason to believe these constant offset terms will remain the same when the magnets are reassembled.

The forward and reconstruction coefficients generated from the model (see Appendix A for tables) can be used for future data analysis since they represent a self–consistent set of coefficients. The model also gives cross–terms which were not obtained in the calibration, while accurately preserving the well measured coefficients. The momentum dependence of the coefficients, particularly in $\langle x_f | \theta_o \rangle$ and $\langle \theta_f | \theta_o \rangle$, can be accounted for in data analysis by fitting the overall effect on the acceptance function and then correcting the data accordingly. The next section addresses this correction.

3.3 Momentum Dependence of the Acceptance

The forward first–order transformation for the bend plane of the spectrometer, for $y_o = 0$, is given by the following linear relations:

$$y_f = \langle y_f | \phi_o \rangle \phi_o + \langle y_f | \delta \rangle \delta \tag{3.4}$$

$$\phi_f = \langle \phi_f | \phi_o \rangle \phi_o + \langle \phi_f | \delta \rangle \delta. \tag{3.5}$$

If we consider a bundle of rays filling an initial volume element $d\phi_o d\delta$, and the corresponding volume element after transport, given by $dy_f d\phi_f$, then the two volume elements are related by the absolute value of the Jacobian,

$$dy_f d\phi_f = |J| d\phi_o d\delta, \tag{3.6}$$

where J is the Jacobian of the transformation. Conservation of the number of particles requires:

$$\int \rho_o(\phi_o \delta) d\phi_o d\delta = \int \rho_f(y_f \phi_f) dy_f d\phi_f, \tag{3.7}$$

where ρ_o and ρ_f are the densities of the rays in the coordinates ϕ_o, δ and y_f, ϕ_f, respectively. Using Equations 3.6 and 3.7, we conclude that

$$\rho_o = \rho_f |J|. \tag{3.8}$$

We identify $|J|^{-1}$ as the acceptance function. Writing J^{-1} explicitly for the bend-plane coefficients gives:

$$J^{-1}_{\phi_o \delta} = \frac{1}{\langle y_f|\delta\rangle\langle\phi_f|\phi_o\rangle - \langle y_f|\phi_o\rangle\langle\phi_f|\delta\rangle}. \tag{3.9}$$

For the non bend-plane, the forward transformation equations are given by:

$$x_f = \langle x_f|x_o\rangle x_o + \langle x_f|\theta_o\rangle\theta_o, \tag{3.10}$$

and

$$\theta_f = \langle\theta_f|x_o\rangle x_o + \langle\theta_f|\theta_o\rangle\theta_o, \tag{3.11}$$

and one can write the Jacobian as:

$$J_{x_o\theta_o} = \langle x_f|x_o\rangle\langle\theta_f|\theta_o\rangle - \langle x_f|\theta_o\rangle\langle\theta_f|x_o\rangle. \tag{3.12}$$

In the x and θ plane the transformation is canonical and this requires that the Jacobian must equal unity. The Jacobian was calculated at each momentum as a check on the data, and was found to equal unity within the errors.

To determine the momentum dependence of the acceptance in the non-bend plane, we consider the rays originating from a fixed value of x_o. We choose $x_o = 0$, but the results will be valid for any fixed value of x_o. The forward first–order transport equations for $x_0 = 0$ become:

$$x_f = \langle x_f|\theta_o\rangle\theta_o, \tag{3.13}$$

and

$$\theta_f = \langle\theta_f|\theta_o\rangle\theta_o. \tag{3.14}$$

Similarly, the reverse transformations can be written as follows, for $x_o = 0$:

$$0 = \langle x_o|x_f\rangle x_f + \langle x_o|\theta_f\rangle\theta_f, \tag{3.15}$$

$$\theta_o = \langle\theta_o|x_f\rangle x_f + \langle\theta_o|\theta_f\rangle\theta_f. \tag{3.16}$$

If we assume that a set of nominal coefficients, denoted by a subscript N, was used to reconstruct the target quantities, then the reconstructed scattering angle, θ_N, is given by:

$$\theta_N = \langle\theta_o|x_f\rangle_N x_f + \langle\theta_o|\theta_f\rangle_N\theta_f. \tag{3.17}$$

Multiplying Equation 3.13 by $\langle\theta_o|x_f\rangle_N$ and equation 3.14 by $\langle\theta_o|\theta_f\rangle_N$ and then adding the equations together, using equation 3.16, gives :

$$\theta_N = \Big[\langle\theta_o|x_f\rangle_N\langle x_f|\theta_o\rangle + \langle\theta_o|\theta_f\rangle_N\langle\theta_f|\theta_o\rangle\Big]\theta_o. \tag{3.18}$$

From this equation we can write the change in θ_o with respect to θ_N as:

$$\frac{d\theta_o}{d\theta_N} = \frac{1}{\langle\theta_o|x_f\rangle_N\langle x_f|\theta_o\rangle + \langle\theta_o|\theta_f\rangle_N\langle\theta_f|\theta_o\rangle}. \tag{3.19}$$

This tells us how the true angle, or the true θ acceptance, changes with respect to the reconstructed angle, or the assumed θ acceptance, which depends on the set of

reconstruction coefficients used in determining θ_N. An equivalent expression is given by;

$$\frac{d\theta_o}{d\theta_N} = \frac{1}{\langle x_f|x_o\rangle_N\langle\theta_f|\theta_o\rangle - \langle\theta_f|x_o\rangle_N\langle x_f|\theta_o\rangle}, \tag{3.20}$$

where the nominal reverse coefficients have been replaced by their forward counterparts. Since the Jacobian is equal to unity, $\langle\theta_o|x_f\rangle = -\langle\theta_f|x_o\rangle$, and, $\langle\theta_o|\theta_f\rangle = \langle x_f|x_o\rangle$.

Figure 3.13 contains plots of the inverse Jacobian versus spectrometer momentum for the ϕ–δ and x–θ acceptances. A plot of the momentum dependence of the total acceptance, A_{total}, is given by the product of the momentum dependence for the ϕ–δ and x–θ acceptances, since to first order they are independent. Equations 3.9 and 3.19 were used to generate each the ϕ–δ and x–θ acceptances respectively, and in each case the points are normalized to the 3 GeV data. For the x–θ plane this means that the nominal set of coefficients are those from the 3 GeV fit. The error bars on the points are statistical and are determined from the Monte Carlo as was the case for the statistical errors for all the coefficients. The systematic error is given by the bar to the left of the first point and it is the same for all points and is perfectly correlated. It therefore indicates a possible shift in magnitude but does not change the shape of the curves.

From these plots, we see that the x–θ acceptance shows a slight momentum dependence indicated by the slope in the data versus momentum. For the vertical plane however, there is no evidence of any momentum dependence to the ϕ–δ acceptance. The slope in the θ acceptance comes directly from the slopes in the forward coefficients, $\langle\theta_f|\theta_o\rangle$ and $\langle x_f|\theta_f\rangle$. This effect was found to be half due to the saturation of the dipoles, and half due to the method used to set the current in the quadrupoles. The quadrupoles were set in the same manner for experiments prior to and including NE11, thus the acceptance functions used in analyzing data from those experiments should be modified to account for the momentum dependence found in the θ acceptance. To find the correction necessary for a given experiment, one must calculate

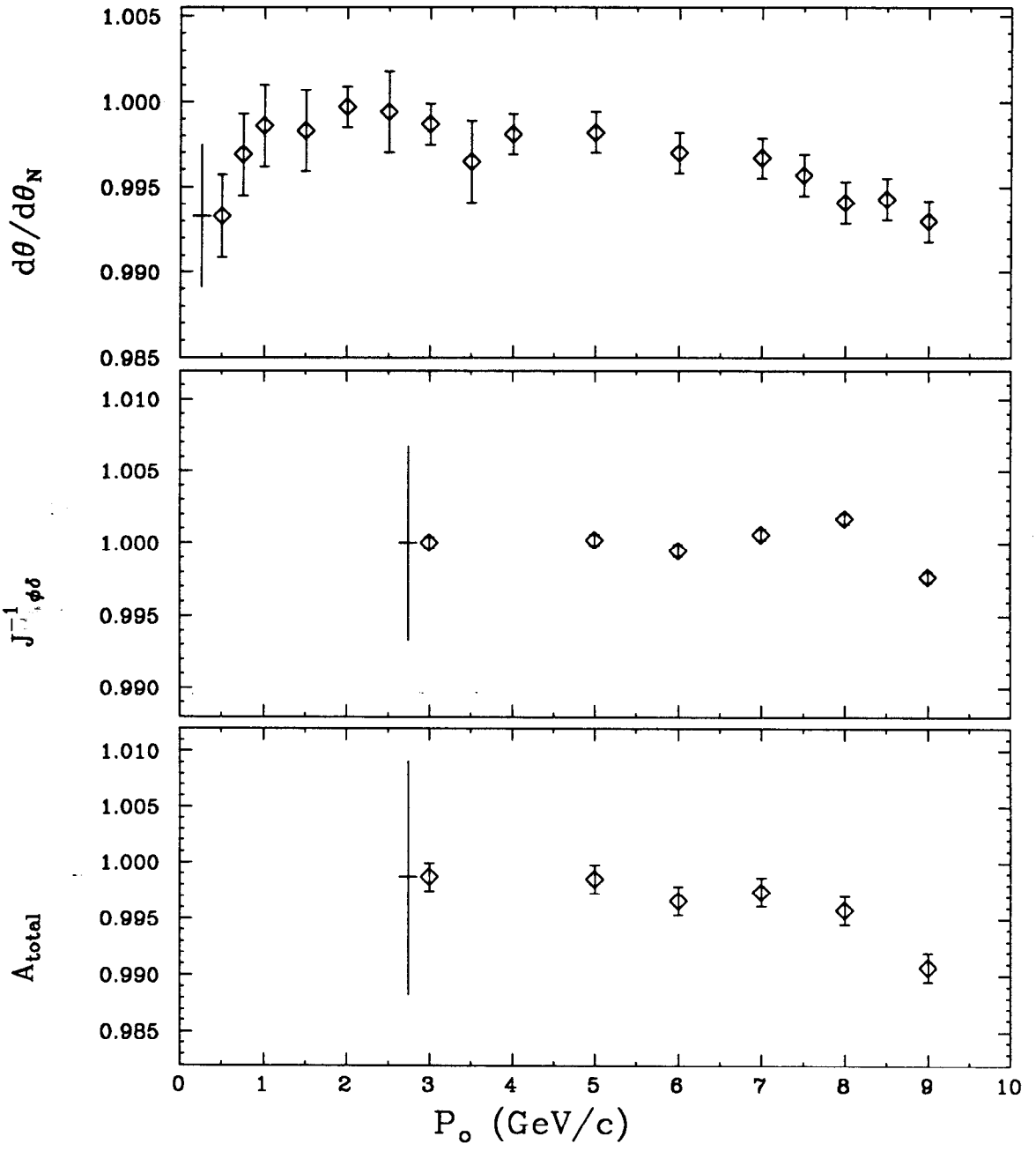

Figure 3.13. The momentum dependence of the acceptance. Shown are plots of the inverse Jacobian determinant for the θ acceptance, the ϕ–δ acceptance, and the total acceptance. A slope in the data indicates a momentum dependence to the acceptance. The errors are statistical with the systematic error to the left of the first point.

both $J^{-1}_{\phi_o\delta}$ and $\frac{d\theta_o}{d\theta_N}$, Equations 3.9 and 3.19 respectively, using the reconstruction coefficients actually used in the analysis as the nominal set, or the set to which the corrections will be normalized. The results can then be fit and multiplied by the acceptance to apply the correction. As an example, Table 3.4 gives the values of these corrections as calculated for E140. Notice that in this case there is a 2% correction needed for the ϕ–δ acceptance. This is due to the set of reconstruction coefficients used in E140, which differed from those measured in the wire float. Note that the systematic uncertainty in these corrections is ± 1.0%. Thus, at best, the acceptance can be determined to within ± 1.0%.

Table 3.4. Acceptance corrections for E140. This is a table of multiplicative correction factors for the θ and ϕ–δ acceptance functions for experiment E140.

ACCEPTANCE CORRECTIONS FOR E140

P_o	$\frac{d\theta}{d\theta_N}$	$J^{-1}_{\phi_o\delta}$	A_{total}
3.0	0.9962	0.9853	0.9810
5.0	0.9957	0.9856	0.9814
6.0	0.9945	0.9849	0.9795
7.0	0.9942	0.9860	0.9803
8.0	0.9916	0.9870	0.9787
9.0	0.9904	0.9831	0.9737
Statistical Uncertainty	± 0.0012	± 0.0004	± 0.0013
Systematic Uncertainty	± 0.0041	± 0.0066	± 0.0100

4. Comments and Conclusions

With regard to the calibration technique, there are a few minor improvements which might increase the precision of future calibrations. As previously mentioned, the use of an air–bearing pulley with a cylindrical axle would eliminate the dependence of the induced tension on the pulley wheel orientation, thereby reducing the problems associated with determining the magnitude of the induced tension. The second improvement would be to clearly mark the plane in **z** in which the wire position is determined at each of the two inner frames. The uncertainty in knowing the exact location of this plane translates directly into the systematic uncertainty in the first–order coefficients. Although the above improvements should, in principle, reduce the systematic errors, the size of the reduction is small. More important than fine tuning and improving the hardware, is to improve the quantity of data, particularly for the bend plane coefficients at momenta less than 3 GeV, and to take accurate and frequent NMR measurements of the dipole fields. It was a lack of precise magnetic field measurements which limited the precision of the fit to central momentum versus magnetic field.

Overall, the wire float calibration achieved its goals. The optics coefficients were obtained for a wide range in momentum and with very high precision. The large, first–order coefficients were measured to better than $\pm$ 0.5%, and the central momentum was calibrated to $\pm$ 0.025% in the worst case. These measurements were then used to determine the momentum dependence of the acceptance and to update a TRANSPORT model of the spectrometer.

Appendix A: Reconstruction Coefficients

The reverse TRANSPORT matrix elements need to be modified before they can be used to reconstruct the target scattering coordinates from the measured hut quantities. In an experiment, the particle's x and y positions and the corresponding angles, θ and ϕ, are measured via the ten planes of wire chambers. In order to obtain the particle's fractional momentum, δ, a constraint, $y = 0$, is applied to the system of linear equations from which the matrix elements are determined. This is consistent with the physical characteristics of the beam at the target, which is approximately 2 mm in y, and it allows one to solve for δ in terms of the remaining coordinates. The details of this calculation and the resulting transformation equations are given below. This derivation is based on Sill's work,[7] the main difference being that in this case TRANSPORT must be run with the usual ordering of $\{x, \theta, y, \phi, l, \delta\}$, and not with y first as in Sill's case. Also, several typing errors appear in Sill's work and these have been corrected here.

Given the equation for the reverse TRANSPORT transformation as $\mathbf{Q} = \mathbf{M_s^{-1}q}$, where for a second order expansion $\mathbf{M_s^{-1}}$ is a six by twenty-seven element matrix, $\mathbf{Q} = \{x_o, \theta_o, y_o, \phi_o, l, \delta\}$, and $\mathbf{q}$ has been expanded to a twenty-seven element vector containing $\{x_f, \theta_f, y_f, \phi_f, l, \delta, ...\}$ plus all cross terms, we wish to set $y_o = 0$ and solve for δ. Thus, we must solve

$$y_o \equiv 0 = \sum_{i=1}^{6} \langle y_o | q_i \rangle q_i + \sum_{i=1}^{6} \sum_{j=1}^{i} \langle y_o | q_i q_j \rangle q_i q_j \qquad (A.1)$$

for δ, which is q_6. If we adopt the notation used by Sill, then we can write the

equation as follows:

$$y_o = 0 = \sum_{i=1}^{4} A(3,i)q_i + A(3,6)\delta + \sum_{i=1}^{4}\sum_{j=1}^{i} B_3(i,j)q_iq_j + \sum_{j=1}^{4} B_3(6,j)q_j\delta + B_3(6,6)\delta^2, \tag{A.2}$$

where, $A(3,i) = \langle y_o|q_i\rangle$ corresponds to the first–order matrix coefficients in the TRANSPORT output and $B_3(i,j) = \langle y_o|q_iq_j\rangle$ corresponds to the second order coefficients. Note that now the sum is written from 1 to 4 since all terms with $i = 5$ vanish and the terms for $i = 6$ have been written explicitly in terms of δ. If we let:

$$a = B_3(6,6), \qquad b = A(3,6) + \sum_{j=1}^{4} B_3(6,j)q_j, \qquad c = c_o + c_1,$$

where

$$c_o = \sum_{i=1}^{4} A(3,i)q_i \qquad \text{and} \qquad c_1 = \sum_{i=1}^{4}\sum_{j=1}^{i} B_3(i,j)q_iq_j \ ,$$

then equation A.2 can be expressed as a quadratic in δ:

$$0 = c + b\delta + a\delta^2 \ . \tag{A.3}$$

Solving for δ after expanding the radical out to second order yields:

$$\delta = -\frac{c}{b}\left(\frac{ac}{b^2} + 1\right). \tag{A.4}$$

This is the physical solution since $A(3,6)$ must be large for bending systems and $B_3(6,6)$ small when the optics are dominated by first order terms. We can then write $b = b_o(1+\epsilon)$ where $b_o = A(3,6)$ and $\epsilon = \sum_{i=1}^{4} B_3(6,i)q_i/b_o$. Then, expanding about ϵ and keeping terms to second order only in q_iq_j gives:

$$\delta = -\frac{c_o^2 a}{b_o^3} - \frac{c_o}{b_o}(1-\epsilon) - \frac{c_1}{b_o}. \tag{A.5}$$

Substituting back the expressions for c_o, c_1, and ϵ and making use of the following index switching relations:

$$\sum_{i=1}^{4}\sum_{j=1}^{4}\alpha_{ij} = \sum_{i=1}^{4}\sum_{j=1}^{i}\alpha_{ij} + \sum_{i=1}^{4}\sum_{j=1+1}^{4}\alpha_{ij}$$

and

$$\sum_{i=1}^{4}\sum_{j=(i+1)}^{4}\alpha_{ij} = \sum_{i=1}^{4}\sum_{j=1}^{i}\alpha_{ji}(1-\delta_{ij})$$

gives the following expression for δ:

$$\begin{aligned}\delta = & -\frac{a}{b_o^3}\sum_{i=1}^{4}\sum_{j=1}^{i}A(3,i)A(3,j)q_iq_j\delta_{ij} - \frac{2a}{b_o^3}\sum_{i=1}^{4}\sum_{j=1}^{i}A(3,i)A(3,j)q_iq_j(1-\delta_{ij}) \\ & + \frac{1}{b_o^2}\sum_{i=1}^{4}\sum_{j=1}^{i}A(3,i)B_3(6,j)q_iq_j + \frac{1}{b_o^2}\sum_{i=1}^{4}\sum_{j=1}^{i}A(3,j)B_3(6,i)q_iq_j(1-\delta_{ij}) \\ & - \frac{1}{b_o}\sum_{i=1}^{4}\sum_{j=1}^{i}B_3(i,j)q_iq_j - \frac{1}{b_o}\sum_{i=1}^{4}A(3,i)q_i.\end{aligned} \tag{A.6}$$

Gathering terms in q_iq_j and q_i separately and substituting back the values of a and b_o gives the following final expressions for reconstructed δ coefficients in terms of the reverse TRANSPORT coefficients for the constraint $y = 0$:

$$\begin{aligned}\langle\delta|q_i\rangle &= \frac{-1}{A(3,6)}A(3,i), \\ \langle\delta|q_iq_j\rangle &= \frac{1}{A^2(3,6)}\{A(3,i)B_3(6,j) + A(3,j)B_3(6,i)(1-\delta_{ij}) \\ &\quad - A(3,6)B_3(i,j) - \frac{A(3,i)A(3,j)B_3(6,6)}{A(3,6)}(2-\delta_{ij})\},\end{aligned} \tag{A.7}$$

where,

$$\delta = \sum_{i=1}^{4}\langle\delta|q_i\rangle q_i + \sum_{i=1}^{4}\sum_{j=1}^{i}\langle\delta|q_iq_j\rangle q_iq_j \tag{A.8}$$

and $q_i = \{x_f, \theta_f, y_f, \phi_f\}$.

To get the expressions for the remaining reconstruction coefficients we must substitute the expansion for δ, given by equation A.8, into the general expression for the

coefficients:

$$Q_k = \sum_{i=1}^{4} A(k,i)q_i + A(k,6)\delta + \sum_{i=1}^{4}\sum_{j=1}^{i} B_k(i,j)q_iq_j + \sum_{j=1}^{4} B_k(6,j)q_j\delta + B_k(6,6)\delta^2 . \tag{A.9}$$

Note that this equation is analogous to equation A.2 which was for y_o. Performing the substitution and retaining terms up to second order in q only gives the following:

$$\begin{aligned} Q_k = & \sum_{i=1}^{4} A(k,i)q_i + \sum_{i=1}^{4}\sum_{j=1}^{i} B_k(i,j)q_iq_j - \frac{A(k,6)}{A(3,6)}\sum_{i=1}^{4} A(3,i)q_i \\ & + \frac{A(k,6)}{A^2(3,6)}\sum_{i=1}^{4}\sum_{j=1}^{i}\{A(3,i)B_3(6,j) + A(3,j)B_3(6,i)(1-\delta_{ij})\}q_iq_j \\ & - \frac{A(k,6)}{A(3,6)}\sum_{i=1}^{4}\sum_{j=1}^{i} B_3(i,j)q_iq_j - \frac{A(k,6)}{A^3(3,6)}\sum_{i=1}^{4}\sum_{j=1}^{i} B_3(6,6)A(3,i)A(3,j)(2-\delta_{ij})q_iq_j \\ & - \frac{1}{A(3,6)}\sum_{i=1}^{4} A(3,i)q_i\sum_{j=1}^{4} B_k(6,j)q_j + \frac{B_k(6,6)}{A^2(3,6)}\sum_{i=1}^{4}\sum_{j=1}^{i} A(3,i)A(3,j)(2-\delta_{ij})q_iq_j . \end{aligned} \tag{A.10}$$

Define $C_{ijk} \equiv B_k(i,j) - \frac{A(k,6)}{A(3,6)}B_3(i,j)$, and gather terms in q_i and q_iq_j separately. The final expressions for the remaining reconstruction coefficients are given by:

$$\begin{aligned} \langle Q_k|q_i\rangle &= A(k,i) - \frac{A(k,6)}{A(3,6)}A(3,i), \\ \langle Q_k|q_iq_j\rangle &= C_{ijk} + \frac{1}{A(3,6)}\{\frac{A(3,i)A(3,j)}{A(3,6)}C_{66k}(2-\delta_{ij}) - \\ & \quad A(3,j)C_{i6k}(1-\delta_{ij}) - A(3,i)C_{6jk}\}, \end{aligned} \tag{A.11}$$

where,

$$Q_k = \sum_{i=1}^{4}\langle Q_k|q_i\rangle q_i + \sum_{i=1}^{4}\sum_{j=1}^{i}\langle Q_k|q_iq_j\rangle q_iq_j, \tag{A.12}$$

and $q_i = \{x_f, \theta_f, y_f, \phi_f, l\}$ and $Q_k = \{x_o, \theta_o, y_o, \phi_o, l\}$.

The value of these transformations is that they allow one to obtain a set of reconstruction coefficients from the output generated from TRANSPORT rather than fitting a set of rays generated via a Monte Carlo or TURTLE. In order to make use of

these equations and arrive at the correct sign for the reconstruction coefficients, the following procedure should be followed:

- Run TRANSPORT with the 8 GeV elements in the reverse order. Keep in mind that the convention employed in TRANSPORT is that a positive bend is in the -x direction. To have the signs work out it is recommended that one introduce a $-90°$ rotation for the dipole magnets. This rotation will automatically give you the correct ordering of the input vector as $\{x_f, \theta_f, y_f, \phi_f, l, \delta\}$.
- Apply Equations A.7 and Equations A.11 to obtain the reconstruction coefficients from the reverse TRANSPORT coefficients.
- Make a 180° rotation about **y** to go from the right handed coordinate system used in TRANSPORT to the right handed coordinate system used for the hut coordinates during analysis. (In all cases the orientation is such that one is standing in the hut looking at the pivot.) Thus, the following sign changes are needed to attain the final reconstruction coefficients in the same coordinate system in which they are measured and used in analysis:

$$\begin{aligned} x &\longrightarrow -x \\ \phi &\longrightarrow -\phi \\ z &\longrightarrow -z. \end{aligned} \qquad (A.13)$$

The above prescription has been applied to the TRANSPORT model given in the text in section 3.2.4. Table A.1 contains the forward TRANSPORT coefficients resulting from the above model, while Table A.2 contains the reverse TRANSPORT coefficients.

Table A.1. Forward coefficients from the new TRANSPORT model. Listed are the forward TRANSPORT coefficients obtained from the model in table 3.2.

FORWARD TRANSPORT COEFFICIENTS AT 3 GeV

	x_f	θ_f	y_f	ϕ_f	ℓ_f	δ
x_o	0.0106	−0.2074	0.0	0.0	0.0	0.0
θ_o	4.5720	4.8813	0.0	0.0	0.0	0.0
y_o	0.0	0.0	−0.9300	−0.8565	0.2645	0.0
ϕ_o	0.0	0.0	−0.0002	−1.0754	0.3184	0.0
ℓ_o	0.0	0.0	0.0	0.0	1.0	0.0
δ	0.0	0.0	−2.9610	0.1173	−0.3954	1.0
$x_o x_o$	0.0	0.0	1.990E-5	1.377E-4	−5.131E-4	0.0
$x_o \theta_o$	0.0	0.0	−1.539E-4	−1.822E-5	1.264E-3	0.0
$x_o y_o$	−1.014E-3	−1.107E-3	0.0	0.0	0.0	0.0
$x_o \phi_o$	1.972E-4	1.744E-4	0.0	0.0	0.0	0.0
$x_o \ell_o$	0.0	0.0	0.0	0.0	0.0	0.0
$x_o \delta$	4.356E-2	4.587E-2	0.0	0.0	0.0	0.0
$\theta_o \theta_o$	0.0	0.0	3.089E-4	−1.616E-3	−7.544E-3	0.0
$\theta_o y_o$	−5.625E-4	1.725E-4	0.0	0.0	0.0	0.0
$\theta_o \phi_o$	−7.639E-4	−6.701E-4	0.0	0.0	0.0	0.0
$\theta_o \ell_o$	0.0	0.0	0.0	0.0	0.0	0.0
$\theta_o \delta$	−1.272E-2	−2.718E-2	0.0	0.0	0.0	0.0
$y_o y_o$	0.0	0.0	4.369E-4	−8.105E-4	−1.873E-3	0.0
$y_o \phi_o$	0.0	0.0	3.908E-5	−9.747E-4	−1.026E-3	0.0
$y_o \ell_o$	0.0	0.0	0.0	0.0	0.0	0.0
$y_o \delta$	0.0	0.0	1.221E-2	−2.553E-2	5.471E-4	0.0
$\phi_o \phi_o$	0.0	0.0	6.695E-7	−2.208E-5	−6.835E-4	0.0
$\phi_o \ell_o$	0.0	0.0	0.0	0.0	0.0	0.0
$\phi_o \delta$	0.0	0.0	1.283E-2	−2.308E-3	3.041E-3	0.0
$\ell_o \ell_o$	0.0	0.0	0.0	0.0	0.0	0.0
$\ell_o \delta$	0.0	0.0	0.0	0.0	0.0	0.0
$\delta \delta$	0.0	0.0	3.136E-3	−4.884E-2	−1.763E-3	0.0

These reverse coefficients are what one obtains when the −90° rotation has been used for the dipole magnets. If one wants to make use of these reverse coefficients keep in mind that they are *not* in the coordinate system normally used in analysis. The sign flips indicated above must be employed in order to get agreement between

Table A.2. Reverse coefficients from the new TRANSPORT model. Listed are the reverse TRANSPORT coefficients obtained from the model in table 3.2.

REVERSE TRANSPORT COEFFICIENTS AT 3 GeV

	x_o	θ_o	y_o	ϕ_o	ℓ_o	δ
x_f	4.8813	−0.2074	0.0	0.0	0.0	0.0
θ_f	4.5720	0.0106	0.0	0.0	0.0	0.0
y_f	0.0	0.0	−1.0754	−0.8565	−0.0117	0.0
ϕ_f	0.0	0.0	−0.0002	−0.9300	0.2961	0.0
ℓ_f	0.0	0.0	0.0	0.0	1.0	0.0
δ	0.0	0.0	−3.1843	−2.6452	−0.3954	1.0
$x_f x_f$	0.0	0.0	3.563E-4	−2.684E-3	−1.032E-2	0.0
$x_f \theta_f$	0.0	0.0	8.047E-4	−5.064E-3	−1.991E-2	0.0
$x_f y_f$	−7.595E-4	1.340E-3	0.0	0.0	0.0	0.0
$x_f \phi_f$	−6.233E-4	1.624E-4	0.0	0.0	0.0	0.0
$x_f \ell_f$	0.0	0.0	0.0	0.0	0.0	0.0
$x_f \delta$	−2.950E-2	4.986E-2	0.0	0.0	0.0	0.0
$\theta_f \theta_f$	0.0	0.0	4.551E-4	−2.314E-3	−9.930E-3	0.0
$\theta_f y_f$	−4.937E-5	1.259E-3	0.0	0.0	0.0	0.0
$\theta_f \phi_f$	−7.103E-4	1.836E-4	0.0	0.0	0.0	0.0
$\theta_f \ell_f$	0.0	0.0	0.0	0.0	0.0	0.0
$\theta_f \delta$	−1.295E-2	4.731E-2	0.0	0.0	0.0	0.0
$y_f y_f$	0.0	0.0	5.052E-4	4.542E-4	−1.734E-3	0.0
$y_f \phi_f$	0.0	0.0	−4.088E-5	−9.062E-4	2.140E-4	0.0
$y_f \ell_f$	0.0	0.0	0.0	0.0	0.0	0.0
$y_f \delta$	0.0	0.0	6.792E-4	−2.294E-2	−7.113E-4	0.0
$\phi_f \phi_f$	0.0	0.0	6.188E-7	1.809E-5	−5.967E-4	0.0
$\phi_f \ell_f$	0.0	0.0	0.0	0.0	0.0	0.0
$\phi_f \delta$	0.0	0.0	1.271E-2	9.532E-3	2.827E-3	0.0
$\ell_f \ell_f$	0.0	0.0	0.0	0.0	0.0	0.0
$\ell_f \delta$	0.0	0.0	0.0	0.0	0.0	0.0
$\delta\delta$	0.0	0.0	2.469E-3	−2.237E-2	−2.824E-3	0.0

the TRANSPORT coordinate system and that used for analysis purposes. Applying equations A.7 and A.11 on the reverse coefficients of table A.2, and then making the sign flips, gives the reconstruction coefficients of Table A.3.

Table A.3. Reconstruction coefficients derived from the new TRANSPORT model. Listed are the reconstruction coefficients for 3 GeV. These were derived under the constraint $y_o = 0$, from the reverse matrix elements given in Table A.2

RECONSTRUCTION COEFFICIENTS AT 3 GeV

	x_o	θ_o	ϕ_o	ℓ_o	δ
x_f	4.8813	0.2074	0.0	0.0	0.0
θ_f	−4.5720	0.0106	0.0	0.0	0.0
y_f	0.0	0.0	−0.0368	0.1218	−0.3377
ϕ_f	0.0	0.0	−0.9299	−0.2961	0.0001
$x_f x_f$	0.0	0.0	2.980E-3	−1.036E-2	1.120E-4
$x_f \theta_f$	0.0	0.0	−5.732E-3	2.001E-2	−2.530E-4
$x_f y_f$	9.203E-3	1.550E-2	0.0	0.0	0.0
$x_f \phi_f$	6.210E-4	1.590E-4	0.0	0.0	0.0
$\theta_f \theta_f$	0.0	0.0	2.692E-3	−9.987E-3	1.430E-4
$\theta_f y_f$	−4.324E-3	−1.472E-2	0.0	0.0	0.0
$\theta_f \phi_f$	−7.090E-4	−1.810E-4	0.0	0.0	0.0
$y_f y_f$	0.0	0.0	−5.187E-3	−1.885E-3	1.750E-4
$y_f \phi_f$	0.0	0.0	−5.250E-4	2.030E-4	1.361E-3
$\phi_f \phi_f$	0.0	0.0	−1.800E-5	−5.970E-4	0.0

Appendix B: Survey of the Frames

The data recorded for the position of each trajectory consisted of an **x** and **y** coordinate at each of the four frames. To convert these arbitrary values into TRANSPORT coordinates the position of the standard reference trajectory, see Section 2.3, was surveyed at each of the four frames, giving the coordinates of the trajectory in a TRANSPORT system. With coordinates given for both TRANSPORT and the internal coordinate system of each frame, establishing the relationship between the two systems was straight forward.

For all measurements made during the floating wire calibration the 8 GeV spectrometer was at 11.5°. The spectrometer center line was nominally defined as the line entering Q81 horizontally at beam height, in a vertical plane containing Tooling Ball A of Q81 and Tooling Ball B of Q83 and exiting the spectrometer at 30° to the horizontal in this same vertical plane. This line defines the TRANSPORT coordinate system and it represents a central ray. Thus **x** measurements denote distances to the left, (+**x**), and right, (−**x**), when facing downstream and **y** measurements are above, (+**y**), and below, (−**y**) this line. The quantity **z** is along the line itself.

The frames at the entrance of the spectrometer were fairly straight forward to calibrate. Frame 1, located at the intersection between beam center line and the north–south transversal,[19] and marked by the point where the wire disappeared into the groove in the pulley, was directly surveyed. A transit on the floor allowed the **y** position of the pulley to be continually monitored, while another above Q82 was used to measure the **x** position. For Frame 2 the situation was complicated by the fact that the cylindrical position sensors obscured the wire and we were forced to survey its location close to, but not exactly at, Frame 2. For the **x** position, this posed no problem as **x** did not vary with **z**, however a correction of 0.018 cm had to be made

to the y measurement to account for the catenary shape of the wire due to its mass.

Surveying the wire position at the frames in the hut was complicated due to the physical constraints of a confined area and an angle of 30° with respect to the horizontal. To overcome these difficulties, the method of triangulation was used to determine the coordinates of the wire at Frame 4, marked by the tangent point on the half–pulley, and three additional points located on the wire. These three points were then used to determine the wire location at Frame 3 via extrapolation, since the wire at Frame 3 was obscured from the transit by the cylindrical position sensors.

B.1 Triangulation

A transit mounted on Tooling Ball B above Q83 was used to first determine the coordinates of two reference points, the North and South CERN sockets. These sockets are located on the cement shielding on Q83 and their coordinates are easily measured. A theodolite was then mounted on each socket in turn and two angle measurements made from each; the vertical angle turned between the horizontal and the point on the wire, ϕ_N and ϕ_S, and the horizontal angle turned between the other CERN socket and the point on the wire, θ_N and θ_S. Figure B.1 illustrates these angles and gives a schematic of the points on the wire.

Given $\{\tilde{x}_N, \tilde{y}_N, \tilde{z}_N\}$, $\{\tilde{x}_S, \tilde{y}_S, \tilde{z}_S\}$, ϕ_N, θ_N, ϕ_S, θ_S, as defined above, the coordinates of an arbitrary point, $\{\tilde{x}, \tilde{y}, \tilde{z}\}$, relative to a level coordinate system centered on Tooling Ball B on Q83 are given by:

$$\begin{aligned}
\tilde{x} &= \tilde{x}_N - V\sin(\beta_N) \qquad \text{or} \qquad \tilde{x} = \tilde{x}_S + W\sin(\beta_S) \\
\tilde{y} &= \tilde{y}_N - V\tan(\phi_N) \qquad \text{and} \qquad \tilde{y} = \tilde{y}_S - W\tan(\phi_S) \\
\tilde{z} &= \tilde{z}_N + V\cos(\beta_N) \qquad \text{or} \qquad \tilde{z} = \tilde{z}_S + W\cos(\beta_S)
\end{aligned}$$

where,

$$\begin{aligned}
V &= T\,\frac{\sin(\theta_S)}{\sin(\theta)}\,, \\
W &= T\,\frac{\sin(\theta_N)}{\sin(\theta)}\,, \\
T &= \frac{\tilde{z}_N - \tilde{z}_S}{\sin(\alpha)}\,,
\end{aligned}$$

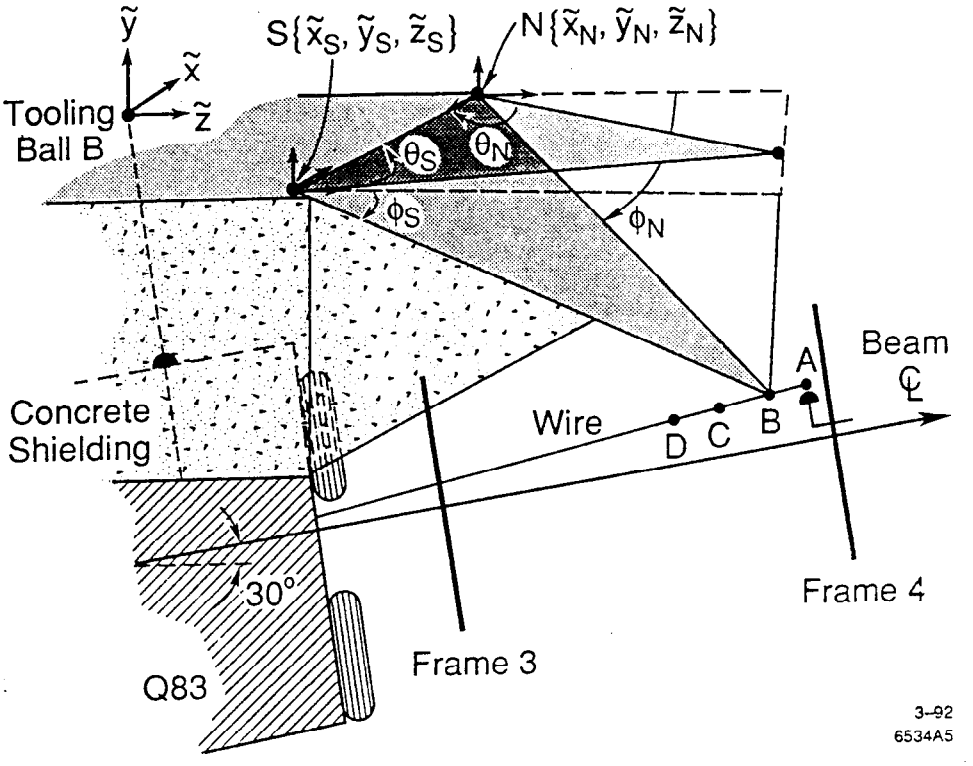

Figure B.1. Triangulation. The letters A–D refer to the four points along the wire. A is the tangent point on the half–pulley, and B, C, and D are points marked by pieces of tape placed on the wire. These points allow extrapolation to Frame 3. The coordinates of these points were obtained for three wire locations corresponding to values of $y_3 = 0$ and $\pm$ 7.62 cm.

$$\alpha = \tan^{-1}\left(\frac{\tilde{z}_N - \tilde{z}_S}{\tilde{x}_N - \tilde{x}_S}\right) ,$$

$$\begin{aligned} \beta_N &= 90 - \theta_N + \alpha , \\ \beta_S &= 90 - \theta_S - \alpha , \\ \theta &= 180 - \theta_N - \theta_S . \end{aligned}$$

Here, all angles are measured in degrees. Conversion to a TRANSPORT coordinate system centered on the downstream exit of Q83 and rotated 30° to the horizontal is given by the equations below.

$$\begin{aligned} x &= \tilde{x} , \\ y &= \tilde{y}\cos(30°) - \tilde{z}\sin(30°) + 79.83982 , \\ z &= \tilde{y}\sin(30°) + \tilde{z}\cos(30°) - 27.68600 . \end{aligned}$$

where measurements of $\tilde{x}$, $\tilde{y}$, and $\tilde{z}$ are in centimeters.

With the coordinates of the three points on the wire determined, extrapolation was used to find the x and y position of the wire at Frame 3. To account for the possibility that the frames might have been skewed, the coordinates of the four points were measured for three different wire trajectories corresponding to $y_3 = 0, \pm 7.62$ cm. A fit to x versus y indicated a small correction was necessary to handle the slight rotation found between frames 3 and 4.

Given the wire location in terms of four pairs of TRANSPORT coordinates, an x, y pair at each frame, the next step was to determine x, θ, y, and ϕ at two points, namely the tangent points of each the air–bearing pulley at the target, and the half–pulley in the hut. To obtain θ and ϕ, the distances between the two sets of frames, $D_{1,2}$ and $D_{3,4}$, was needed. These distances were measured using a steel tape. The relatively large uncertainty in measuring these distances was due to the ambiguity in determining the exact location of the plane in which the inductors sensed the EMF. Lastly, the coordinates of the wire at the half–pulley were extrapolated back to the nominal[20] location for the momentum focal plane of 5.420 m downstream from the magnetic center of Q83.

B.2 Uncertainties in the Surveyed Quantities

Although the frames provided very precise means of measuring the relative position of the wire, the survey method used to convert to TRANSPORT introduced comparatively large uncertainties in the absolute positions. However, the uncertainties in the hut survey quantities were at the minimum achievable level. Table B.1 lists the uncertainties in the raw survey quantities. The dominant uncertainty[21] stems from an uncertainty in knowing the location of the coordinate system centered on Tooling Ball B relative to beam height and beam center line. This uncertainty translates into systematic uncertainties in the position of the north and south CERN sockets.

Table B.1. Uncertainties in hut survey. The uncertainties in the hut survey were at the minimum achievable level. The systematic uncertainties in $\tilde{x}_N$ and $\tilde{x}_S$ are perfectly correlated as are those of $\tilde{y}_N$ and $\tilde{y}_S$, and $\tilde{z}_N$ and $\tilde{z}_S$. These are due to the uncertainty in the location of the coordinate system origin.

HUT SURVEY UNCERTAINTIES

Quantity	Statistical Uncertainty (±)	Systematic Uncertainty (±)
The North and South CERN Sockets		
$\tilde{x}_N$, $\tilde{x}_S$	0.0127 cm	0.0254 cm
$\tilde{y}_N$, $\tilde{y}_S$	0.0127 cm	0.0508 cm
$\tilde{z}_N$, $\tilde{z}_S$	0.0127 cm	0.0254 cm
Points A and B		
θ_N, θ_S	0.0015°	–
ϕ_N, ϕ_S	0.0040°	–
Points C and D		
θ_N, θ_S	0.0025°	–
ϕ_N, ϕ_S	0.0050°	–

Appendix C: The Mass Correction

To correct for the fact that the measurements pertained to massive wires, the current in the wire and coordinates of the wire at the inner frames were adjusted to values which corresponded to a massless wire. To do this, trajectories for both the measured massive wire, and a massless wire with the same initial and final endpoints, were calculated numerically. The current within the massless wire was then varied using a least squares minimization technique until the difference between the massive and massless trajectories was minimized at thirteen points along the trajectory. When this condition was satisfied, the current in the massive wire and the coordinates at the inner frames were replaced by those corresponding to the massless wire.

The model used magnetic fields and drift distances given in the TRANSPORT model of the 8 GeV spectrometer developed from the 1968 beam data.[22] The spectrometer was divided into thirteen segments beginning with Frame 1 and ending at Frame 4. Given the initial position and slope of the wire at the pulley, in both the vertical and horizontal planes, the program used a fourth order Runge–Kutta[23] integration method to solve the equations of motion for the wire in three dimensions. Table C.1 gives the typical size of the correction needed for the current and inner coordinates for both weights. Changes to the x coordinates are $+$ or $-$ depending on which side of the central trajectory a given trajectory lay.

A check of the accuracy of the correction can be made by comparing mass corrected data taken with the 410 g weight versus data taken with the 100 g weight where the correction is four times as great. In the horizontal plane, we can compare results for the $\langle x_f|\theta_o\rangle$ and $\langle\theta_f|\theta_o\rangle$ coefficients. Figure A.1 shows these coefficients before the data for the large and small weight were averaged at 2.0, 3.0 and 4.0 GeV. This plot shows the excellent agreement for results obtained using the two different

Table C.1. This table gives the typical changes in the current and coordinates for the mass correction. The corrections for the 100 g weight are four times as great as expected.

TYPICAL SIZE OF MASS CORRECTION

Quantity	410 g Weight	100 g Weight
I	+ 0.7%	+ 3.0 %
y_2	+ 0.1 cm	+ 0.4 cm
y_3	+ 0.03 cm	+ 0.12 cm
x_2 (x_1= 0)	± 0.003 cm	± 0.013 cm
x_3 (x_1= 0)	± 0.012 cm	± 0.048 cm

masses. In the vertical plane, where the magnitude of the correction is greatest, the best illustration of the agreement obtained between the two weights, and thus a check on the accuracy of the mass correction, comes from comparing wire trajectories before and after the mass correction for both the 410 g and 100 g weights. Figure A.2 contains plots of the y_2 position of each trajectory versus the percentage deviation of current in the trajectory from the central ray current, I_o. The upper plot shows data for the 100 g and 410 g weight prior to applying a mass correction, while the lower plot shows the same data after applying the mass correction. The excellent agreement found in all comparisons is strong evidence that the mass correction was done correctly.

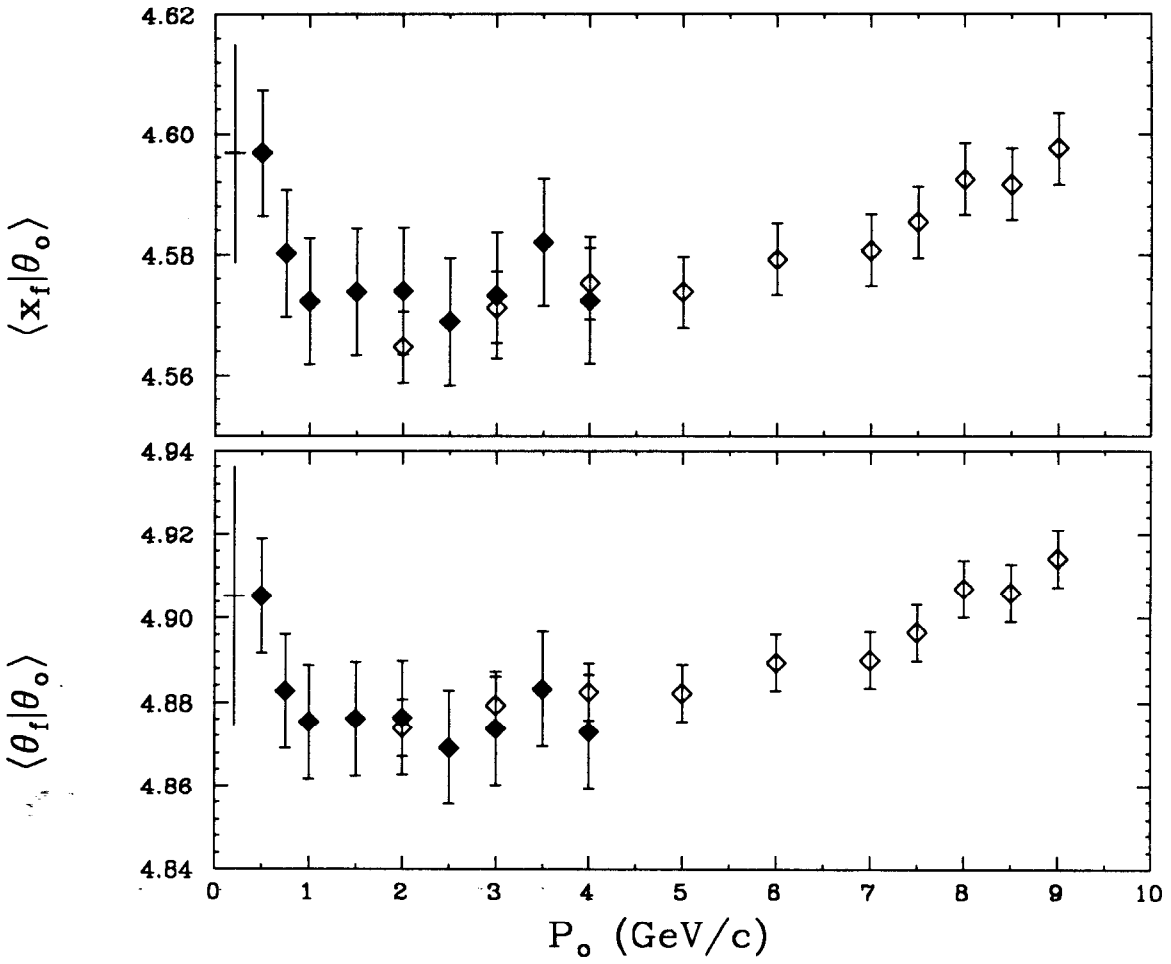

Figure C.1. Accuracy of the mass correction in the horizontal plane. Shown are the forward $\langle x_f|\theta_o\rangle$ and $\langle \theta_f|\theta_o\rangle$ measured coefficients, given in Figure 3.3, *prior* to averaging the 100 g and 410 g data at 2.0, 3.0, and 4.0 GeV. The solid diamonds are the 100 g data, the open diamonds the 410 g data. The error bars on the points are statistical and give the point–to–point fluctuation. The systematic uncertainty is given by the bar to the left of the first point. It is the same for all points and is perfectly correlated. The agreement illustrated in these measurements indicates the accuracy of the mass correction, which was four times as large for the 100 g data.

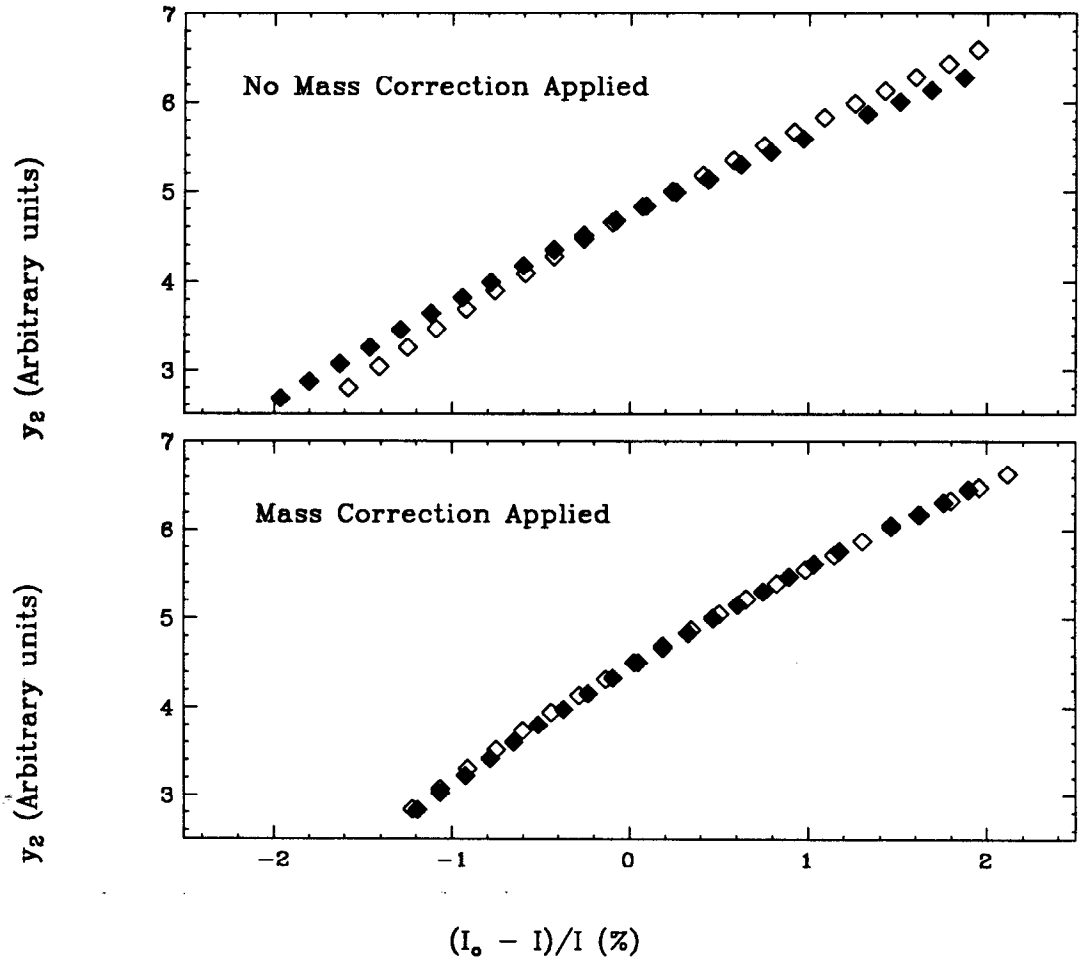

Figure C.2. Accuracy of the mass correction for the vertical plane. These plots illustrate the level of agreement found between the 100 g data, the solid diamonds, and the 410 g data, the open diamonds, once the mass correction has been applied. The upper diagram shows data *prior* to applying the mass correction. The lower plot is the same data after the mass correction. As expected, no difference between the 100 g and 410 g data is seen once the correction has been made.

Appendix D: Tables of Optics Coefficients

Table D.1 contains the forward and reconstruction optics coefficients measured in the wire float. The total error is the quadrature sum of the statistical and systematic.

Table D.1. Forward and reconstruction coefficients as measured in the wire float. Plots of the coefficients versus P_o are given in Section 3.2.

FORWARD COEFFICIENTS

P_o	$\langle x_f \vert \theta_o \rangle$	σ_{stat}	σ_{sys}	σ_{total}
0.50	4.59678	0.01048	0.01810	0.02092
0.75	4.58029	0.01048	0.01810	0.02092
1.00	4.57230	0.01048	0.01810	0.02092
1.50	4.57380	0.01048	0.01810	0.02092
2.00	4.56697	0.00591	0.01810	0.01904
2.50	4.56893	0.01048	0.01810	0.02092
3.00	4.57177	0.00591	0.01810	0.01904
3.50	4.58209	0.01048	0.01810	0.02092
4.00	4.57456	0.00591	0.01810	0.01904
5.00	4.57380	0.00591	0.01809	0.01903
6.00	4.57920	0.00591	0.01809	0.01903
7.00	4.58073	0.00591	0.01809	0.01903
7.50	4.58539	0.00591	0.01809	0.01903
8.00	4.59241	0.00591	0.01809	0.01903
8.50	4.59155	0.00591	0.01809	0.01903
9.00	4.59751	0.00591	0.01809	0.01903
P_o	$\langle \theta_f \vert \theta_o \rangle$	σ_{stat}	σ_{sys}	σ_{total}
0.50	4.90523	0.01357	0.03072	0.03358
0.75	4.88271	0.01357	0.03072	0.03358
1.00	4.87531	0.01357	0.03072	0.03358

continued

Forward coefficients continued

1.50	4.87605	0.01357	0.03072	0.03358
2.00	4.87436	0.00679	0.03072	0.03146
2.50	4.86914	0.01357	0.03072	0.03358
3.00	4.87823	0.00679	0.03072	0.03146
3.50	4.88319	0.01357	0.03072	0.03358
4.00	4.88059	0.00679	0.03072	0.03146
5.00	4.88216	0.00679	0.03065	0.03139
6.00	4.88948	0.00679	0.03065	0.03139
7.00	4.89007	0.00679	0.03065	0.03139
7.50	4.89661	0.00679	0.03065	0.03139
8.00	4.90699	0.00679	0.03065	0.03139
8.50	4.90600	0.00679	0.03065	0.03139
9.00	4.91416	0.00679	0.03065	0.03139

P_o	$\langle x_f \vert x_o \rangle$	σ_{stat}	σ_{sys}	σ_{total}
2.00	0.00436	0.00141	0.01321	0.01329
3.00	0.00992	0.00141	0.01321	0.01329
4.00	0.01343	0.00141	0.01321	0.01329
5.00	0.01074	0.00141	0.01321	0.01329
6.00	0.01233	0.00141	0.01321	0.01329
7.00	0.01287	0.00141	0.01321	0.01329
7.50	0.01548	0.00141	0.01321	0.01329
8.00	0.01048	0.00141	0.01321	0.01329
8.50	0.01035	0.00141	0.01321	0.01329
9.00	0.00537	0.00141	0.01321	0.01329

P_o	$\langle \theta_f \vert x_Q \rangle$	σ_{stat}	σ_{sys}	σ_{total}
2.00	−0.21322	0.00176	0.01415	0.01426
3.00	−0.20748	0.00176	0.01415	0.01426
4.00	−0.20417	0.00176	0.01415	0.01426
5.00	−0.20676	0.00176	0.01415	0.01426
6.00	−0.20511	0.00176	0.01415	0.01426
7.00	−0.20485	0.00176	0.01415	0.01426
7.50	−0.20148	0.00176	0.01415	0.01426
8.00	−0.20650	0.00176	0.01415	0.01426
8.50	−0.20642	0.00176	0.01415	0.01426
9.00	−0.21166	0.00176	0.01415	0.01426

continued

Forward coefficients continued

P_o	$\langle x_f \vert 1 \rangle$	σ_{stat}	σ_{sys}	σ_{total}
2.00	−0.77107	0.01904	0.26239	0.26308
3.00	−0.72536	0.01904	0.26239	0.26308
4.00	−0.71612	0.01904	0.26239	0.26308
5.00	−0.67039	0.01904	0.26239	0.26308
6.00	−0.63373	0.01904	0.26239	0.26308
7.00	−0.56940	0.01904	0.26239	0.26308
7.50	−0.53255	0.01904	0.26239	0.26308
8.00	−0.49741	0.01904	0.26239	0.26308
8.50	−0.43297	0.01904	0.26239	0.26308
9.00	−0.42364	0.01904	0.26239	0.26308
P_o	$\langle \theta_f \vert 1 \rangle$	σ_{stat}	σ_{sys}	σ_{total}
2.00	−0.90398	0.02438	0.30735	0.30832
3.00	−0.85930	0.02438	0.30735	0.30832
4.00	−0.84748	0.02438	0.30735	0.30832
5.00	−0.80673	0.02438	0.30735	0.30832
6.00	−0.76362	0.02438	0.30735	0.30832
7.00	−0.70316	0.02438	0.30735	0.30832
7.50	−0.66788	0.02438	0.30735	0.30832
8.00	−0.62419	0.02438	0.30735	0.30832
8.50	−0.55951	0.02438	0.30735	0.30832
9.00	−0.54549	0.02438	0.30735	0.30832
P_o	$\langle y_f \vert \delta \rangle$	σ_{stat}	σ_{sys}	σ_{total}
3.00	−2.95817	0.00059	0.00550	0.00553
5.00	−2.95988	0.00059	0.00550	0.00553
6.00	−2.95989	0.00059	0.00550	0.00553
7.00	−2.95753	0.00059	0.00550	0.00553
8.00	−2.95244	0.00059	0.00550	0.00553
9.00	−2.95191	0.00059	0.00550	0.00553
P_o	$\langle \phi_f \vert \delta \rangle$	σ_{stat}	σ_{sys}	σ_{total}
3.00	0.17082	0.00286	0.00104	0.00304
5.00	0.17629	0.00286	0.00104	0.00304
6.00	0.17522	0.00286	0.00104	0.00304
7.00	0.16867	0.00286	0.00104	0.00304
8.00	0.17776	0.00286	0.00104	0.00304
9.00	0.17503	0.00286	0.00104	0.00304

continued

Forward coefficients continued

P_o	$\langle y_f \vert \phi_o \rangle$	σ_{stat}	σ_{sys}	σ_{total}
3.00	−0.00012	0.00006	0.00122	0.00122
5.00	−0.00064	0.00006	0.00122	0.00122
6.00	−0.00100	0.00006	0.00122	0.00122
7.00	−0.00125	0.00006	0.00122	0.00122
8.00	−0.00356	0.00006	0.00122	0.00122
9.00	−0.00336	0.00006	0.00122	0.00122
P_o	$\langle \phi_f \vert \phi_o \rangle$	σ_{stat}	σ_{sys}	σ_{total}
3.00	−1.07899	0.00043	0.00696	0.00697
5.00	−1.07807	0.00043	0.00696	0.00697
6.00	−1.07881	0.00043	0.00696	0.00697
7.00	−1.07847	0.00043	0.00696	0.00697
8.00	−1.07903	0.00043	0.00696	0.00697
9.00	−1.08357	0.00043	0.00696	0.00697
P_o	$\langle y_f \vert \delta^2 \rangle$	σ_{stat}	σ_{sys}	σ_{total}
3.00	0.00322	0.00016	0.00031	0.00035
5.00	0.00350	0.00016	0.00031	0.00035
6.00	0.00398	0.00016	0.00031	0.00035
7.00	0.00378	0.00016	0.00031	0.00035
8.00	0.00482	0.00016	0.00031	0.00035
9.00	0.00579	0.00016	0.00031	0.00035
P_o	$\langle \phi_f \vert \delta^2 \rangle$	σ_{stat}	σ_{sys}	σ_{total}
3.00	−0.04854	0.00115	0.00049	0.00125
5.00	−0.04887	0.00115	0.00049	0.00125
6.00	−0.04915	0.00115	0.00049	0.00125
7.00	−0.04704	0.00115	0.00049	0.00125
8.00	−0.04642	0.00115	0.00049	0.00125
9.00	−0.04533	0.00115	0.00049	0.00125
P_o	$\langle y_f \vert \phi_o \delta^2 \rangle$	σ_{stat}	σ_{sys}	σ_{total}
3.00	0.01286	0.00003	0.00008	0.00009
5.00	0.01286	0.00003	0.00008	0.00009
6.00	0.01293	0.00003	0.00008	0.00009
7.00	0.01268	0.00003	0.00008	0.00009
8.00	0.01218	0.00003	0.00008	0.00009
9.00	0.01103	0.00003	0.00008	0.00009

continued

Forward coefficients continued

P_o	$\langle\phi_f\|\phi_o\delta\rangle$	σ_{stat}	σ_{sys}	σ_{total}
3.00	−0.00176	0.00026	0.00008	0.00027
5.00	−0.00214	0.00026	0.00008	0.00027
6.00	−0.00183	0.00026	0.00008	0.00027
7.00	−0.00235	0.00026	0.00008	0.00027
8.00	−0.00259	0.00026	0.00008	0.00027
9.00	−0.00316	0.00026	0.00008	0.00027

RECONSTRUCTION COEFFICIENTS

P_o	$\langle x_o\|\theta_f\rangle$	σ_{stat}	σ_{sys}	σ_{total}
2.00	−4.58805	0.01598	0.02612	0.03062
3.00	−4.58444	0.01598	0.02612	0.03062
4.00	−4.57183	0.01598	0.02612	0.03062
5.00	−4.58010	0.01598	0.02612	0.03062
6.00	−4.57791	0.01598	0.02612	0.03062
7.00	−4.57091	0.01598	0.02612	0.03062
7.50	−4.58283	0.01598	0.02612	0.03062
8.00	−4.59420	0.01598	0.02612	0.03062
8.50	−4.59364	0.01598	0.02612	0.03062
9.00	−4.59792	0.01598	0.02612	0.03062

P_o	$\langle\theta_o\|\theta_f\rangle$	σ_{stat}	σ_{sys}	σ_{total}
2.00	0.00543	0.00157	0.01354	0.01363
3.00	0.01132	0.00157	0.01354	0.01363
4.00	0.01502	0.00157	0.01354	0.01363
5.00	0.01206	0.00157	0.01354	0.01363
6.00	0.01408	0.00157	0.01354	0.01363
7.00	0.01410	0.00157	0.01354	0.01363
7.50	0.01699	0.00157	0.01354	0.01363
8.00	0.01217	0.00157	0.01354	0.01363
8.50	0.01245	0.00157	0.01354	0.01363
9.00	0.00726	0.00157	0.01354	0.01363

continued

Reconstruction coefficients continued

P_o	$\langle x_o \vert x_f \rangle$	σ_{stat}	σ_{sys}	σ_{total}
2.00	4.91398	0.01706	0.01860	0.02524
3.00	4.90841	0.01706	0.01860	0.02524
4.00	4.89597	0.01706	0.01860	0.02524
5.00	4.90488	0.01706	0.01860	0.02524
6.00	4.90391	0.01706	0.01860	0.02524
7.00	4.89596	0.01706	0.01860	0.02524
7.50	4.91113	0.01706	0.01860	0.02524
8.00	4.92697	0.01706	0.01860	0.02524
8.50	4.92479	0.01706	0.01860	0.02524
9.00	4.93217	0.01706	0.01860	0.02524
P_o	$\langle \theta_o \vert x_f \rangle$	σ_{stat}	σ_{sys}	σ_{total}
2.00	0.21274	0.00160	0.01436	0.01445
3.00	0.20694	0.00160	0.01436	0.01445
4.00	0.20288	0.00160	0.01436	0.01445
5.00	0.20606	0.00160	0.01436	0.01445
6.00	0.20350	0.00160	0.01436	0.01445
7.00	0.20351	0.00160	0.01436	0.01445
7.50	0.20006	0.00160	0.01436	0.01445
8.00	0.20508	0.00160	0.01436	0.01445
8.50	0.20482	0.00160	0.01436	0.01445
9.00	0.20984	0.00160	0.01436	0.01445
P_o	$\langle \phi_o \vert y_f \rangle$	σ_{stat}	σ_{sys}	σ_{total}
3.00	−0.04961	0.00090	0.00085	0.00124
5.00	−0.05061	0.00090	0.00085	0.00124
6.00	−0.05033	0.00090	0.00085	0.00124
7.00	−0.04888	0.00090	0.00085	0.00124
8.00	−0.05192	0.00090	0.00085	0.00124
9.00	−0.05139	0.00090	0.00085	0.00124
P_o	$\langle \delta \vert y_f \rangle$	σ_{stat}	σ_{sys}	σ_{total}
3.00	−0.33818	0.00004	0.00064	0.00064
5.00	−0.33803	0.00004	0.00064	0.00064
6.00	−0.33813	0.00004	0.00064	0.00064
7.00	−0.33818	0.00004	0.00064	0.00064
8.00	−0.33887	0.00004	0.00064	0.00064
9.00	−0.33846	0.00004	0.00064	0.00064

continued

Reconstruction coefficients continued

P_o	$\langle\phi_o\|\phi_f\rangle$	σ_{stat}	σ_{sys}	σ_{total}
3.00	−0.92481	0.00031	0.00602	0.00603
5.00	−0.92497	0.00031	0.00602	0.00603
6.00	−0.92458	0.00031	0.00602	0.00603
7.00	−0.92474	0.00031	0.00602	0.00603
8.00	−0.92385	0.00031	0.00602	0.00603
9.00	−0.92012	0.00031	0.00602	0.00603
P_o	$\langle\delta\|\phi_f\rangle$	σ_{stat}	σ_{sys}	σ_{total}
3.00	−0.00038	0.00002	0.00042	0.00042
5.00	−0.00030	0.00002	0.00042	0.00042
6.00	−0.00017	0.00002	0.00042	0.00042
7.00	−0.00012	0.00002	0.00042	0.00042
8.00	0.00059	0.00002	0.00042	0.00042
9.00	0.00079	0.00002	0.00042	0.00042
P_o	$\langle\phi_o\|y_f^2\rangle$	σ_{stat}	σ_{sys}	σ_{total}
3.00	−0.00554	0.00012	0.00004	0.00013
5.00	−0.00559	0.00012	0.00004	0.00013
6.00	−0.00556	0.00012	0.00004	0.00013
7.00	−0.00532	0.00012	0.00004	0.00013
8.00	−0.00528	0.00012	0.00004	0.00013
9.00	−0.00518	0.00012	0.00004	0.00013
P_o	$\langle\delta\|y_f^2\rangle$	σ_{stat}	σ_{sys}	σ_{total}
3.00	0.00017	0.00001	0.00001	0.00001
5.00	0.00018	0.00001	0.00001	0.00001
6.00	0.00021	0.00001	0.00001	0.00001
7.00	0.00020	0.00001	0.00001	0.00001
8.00	0.00022	0.00001	0.00001	0.00001
9.00	0.00026	0.00001	0.00001	0.00001
P_o	$\langle\phi_o\|y_f\phi_f\rangle$	σ_{stat}	σ_{sys}	σ_{total}
3.00	−0.00040	0.00007	0.00002	0.00007
5.00	−0.00041	0.00007	0.00002	0.00007

continued

Reconstruction coefficients continued

6.00	−0.00039	0.00007	0.00002	0.00007
7.00	−0.00055	0.00007	0.00002	0.00007
8.00	−0.00062	0.00007	0.00002	0.00007
9.00	−0.00084	0.00007	0.00002	0.00007
P_o	$\langle\delta\|y_f\phi_f\rangle$	σ_{stat}	σ_{sys}	σ_{total}
3.00	0.00139	0.00000	0.00001	0.00001
5.00	0.00139	0.00000	0.00001	0.00001
6.00	0.00139	0.00000	0.00001	0.00001
7.00	0.00137	0.00000	0.00001	0.00001
8.00	0.00132	0.00000	0.00001	0.00001
9.00	0.00120	0.00000	0.00001	0.00001

References

1. R. C. Walker *et al.*, Phys. Lett. **B224**, 353 (1989); **B240**, 522 (1990).

2. S. Dasu *et al.*, Phys. Rev. Lett. **61,** 1061 (1988).

3. S. Dasu *et al.*, Phys. Rev. Lett. **60,** 2591 (1988).

4. P. E. Bosted *et al.*, submitted to Phys. Rev. Lett. (1992); SLAC-PUB-5744, (1992).

5. D. Coward and G. C. Hartmann, Group A Memo, August (1968).

6. G. C. Hartmann, Group A Memo, August (1968).

7. A. F. Sill, SLAC Technical Note, SLAC NPAS-TN-86-1 (1986).

8. NPAS Users Guide, SLAC-Report-269 (1984).

9. L. Mo and C. Peck, SLAC Technical Note, SLAC-TN-65-29, April, (1965).

10. J. G. Gomez, Ph.D. thesis, American University, unpublished (1987).

11. K. L. Brown *et al.*, SLAC-Report-91, Rev. 2 (1977).

12. K. L. Brown, SLAC-Report-75, Rev. 4 (1982).

13. L. G. Ratner and R. J. Lari, Proceedings of the International Symposium on Magnet Technology, Brechna and Gordon, Eds., 497, (1965).

14. U. Vogel, Rev. Sci. Inst., Vol. 36, (1965).

15. For detailed descriptions of similar apparatus see both H. Bichsel, Proceedings of the International Symposium on Magnet Technology, Brechna and Gordon, Eds., 467, (1965) and Z. F. Wang, S. J. Greene, and M. A. Plum, Nucl. Instru. and Meth. **A243**, 413, (1986).

16. H. Bichsel, Proceedings of the International Symposium on Magnet Technology, Brechna and Gordon, Eds., 467, (1965).

17. J. Cobb and D. Jensen, private communication, (1992).

18. Bill O'Hanlon, 1982 Survey of 8 GeV, (1982).

19. J. M. Lambert, NPAS Technical note, (1983/1984).

20. This value comes from the 1968 survey.

21. Bill O'Hanlon, private communication, (1989).

22. E. M. Riordan, Ph.D. thesis, Massachusetts Institute of Technology, MIT-LNS RX-648 (1973).

23. S. Conte and Carl de Boor, *Elementary Numerical Analysis–An Algorithmic Approach*, Magraw-Hill, 3rd. Ed., 362, (1980).